2018

Nondestructive Testing Methods Aided Via Numerical Computation Models for Various Critical Aerospace Power Generation Systems

Peter Warren
University of Central Florida

NONDESTRUCTIVE TESTING METHODS AIDED VIA NUMERICAL COMPUTATION MODELS FOR VARIOUS CRITICAL AEROSPACE AND POWER GENERATION SYSTEMS

by

PETER OVE WARREN
B.S. Mechanical Engineering
University of Central Florida
Spring 2017

A thesis submitted in partial fulfilment of the requirements
for the degree of Master of Science
in the Department of Mechanical and Aerospace Engineering
in the College of Engineering and Computer Science
at the University of Central Florida
Orlando, Florida

Summer Term
2018

Major Professor: Ranajay Ghosh

ABSTRACT

A current critical necessity for all industries which utilize various equipment that operates in high temperature and extreme environments, is the ability to collect and analyze data via non destructive testing (NDT) methods. Operational conditions and material health must be constantly monitored if components are to be implemented precisely to increase the overall performance and efficiency of the process. Currently in both aerospace and power generation systems there are many methods that are being employed to gather several necessary properties and parameters of a given system. This work will focus primarly on two of these NDT methods, with the ultimate goal of contributing to not only the method itself, but also the role of numerical computation to increase the resolution of a given technique. Numerical computation can attribute knowledge onto the governing mechanics of these NDT methods, many of which are currently being utilized in industry. An increase in the accuracy of the data gathered from NDT methods will ultimately lead to an increase in operational efficiency of a given system.

The first method to be analyzed is a non destructive emmision technique widely referred to as accoustic ultrasonic thermography. This work will investigate the mechanism of heat generation in acoustic thermography using a combination of numerical computational analysis and physical experimentation. Many of the challenges typical of this type of system are addressed in this work. The principal challenges among them are crack detection threshold, signature quality and the effect of defect interactions. Experiments and finite element based numerical simulations are employed, in order to evaluate the proposed method, as well as draw conclusions on the viability for future extension and integration with other digital technologies for health monitoring. A method to determine the magnitude of the different sources of heat generation during an acoustic excitation is also achieved in this work. Defects formed through industrial operation as well as defects formed through artificial manufacturing methods were analyzed and compared.

The second method is a photoluminescence piezospectroscopic (PLPS) for composite materials. The composite studied in this work has one host material which does not illuminate or have photoluminescence properties, the second material provides the luminescence properties, as well as additional overall strength to the composite material. Understanding load transfer between the reinforcements and matrix materials that constitute these composites hold the key to elucidating their mechanical properties and consequent behavior in operation. Finite element simulations of loading effects on representative embedded alumina particles in a matrix were investigated and compared with experimental results. The alumina particles were doped with chromium in order to achieve luminscence capability, and therefore take advantage of the piezospectrscopic measurement technique. Mechanical loading effects on alumina nanoparticle composites can be captured with Photo stimulated luminescent spectroscopy, where spectral shifts from the particles are monitored with load. The resulting piezospectroscopic (PS) coefficients are then used to calculate load transfer between the matrix and particle. The results from the simulation and experiments are shown to be in general agreement of increase in load transferred with increasing particle volume fraction due to contact stresses that are dominant at these higher volume fractions. Results from this work present a combination of analytical and experimental insight into the effect of particle volume fraction on load transfer in ceramic composites that can serve to determine properties and eventually optimize various parameters such as particle shape, size and dispersion that govern the design of these composites prior to manufacture and testing.

This work is dedicated to the administration of Midlothian High School

ACKNOWLEDGMENTS

First, I give my gratitude to my son Ethan, the prophecy foretells that he is to be the stallion who will mount the world. I would also like to express my appreciation to my research advisor and thesis chair, Dr. Ranajay Ghosh, who has been an incredible advisor, an excellent motivator, and has helped me countinuously and selflessly during my graduate acedemic career. I also give my gratitude to my thesis committee members Dr. Seetha Raghavan and Dr. Jihua Gou for their advice, contributions, and support. I also must give my gratitude to Siemens for their many contributions, as they allowed me to use their equipment, and have allowed me the opportunity to work with many of their brilliant engineers. Finally I must thank all of my colleagues here at the University of Central Florida who assisted me in a variety of ways on my many projects.

TABLE OF CONTENTS

LIST OF FIGURES

LIST OF TABLES

CHAPTER 1: INTRODUCTION

Background

Nondestructive testing, widely known as NDT, has served mankind very well over the course of history, and has both grown and evolved at a comparable rate to our understanding of the physical universe. A very primitive definition of nondestructive testing would be the ability to extract some information from a system while inflicting minimal or no damage to the system during the extraction of this information. This desired information could be material properties, the presence of defects, the health of the material, the age of the material, and there is certain to be many more possibilities. This particular branch of science has grown very rapidly over the past 30 years, and must continue to keep pace with the technological evolutions that have and are still currently transforming many fields of engineering and science. If the number of acronyms are any sign or indication of the amount of attention a field of study has recieved than it is certain that this field is doing quite well. There is nondestructive evaluation (NDE), nondestructive inspection (NDI), nondestructive evaluation (NDE), and of course my personal favorite nondestuctive testing (NDT). The repeating word in these acronyms seems to be nondestructive, and this is because it is extremely critical that whatever method is chosen to inspect the component of interest must not be destroyed or have any damage inflicted upon it [1, 2].

NDT has found its way into a variety of fields over the years and is used everyday by many people. A carpenter is able to easily find a stud utilizing sonic energy, and this carpenter doesnt require any understanding of the underlying physics to complete this task. Electromagnetic radiation is passed through us by a doctor when we manage to hurt ourselves and need verification that a bone has been damaged or broken. High speed beverage can manufacturing lines have implemented a variety of optical measurements to verify that the cans being manufactured will be suitable to hold

whatever beverage is set to be stored within them. All of these techniques are examples of NDT methods. The oldest tools used for performing a NDT are of course our senses. Our eyes are constantly used to perform visual inspections, such as making sure that a tire has sufficient air before starting a road trip. NDT is used on the buildings we live in, bridges we drive on, cars we drive in, planes we fly on, and trains we ride in. To summarize, NDT is a critical task for the determination of a variety of information of a given system or component, and is used across a wide variety of fields [3, 4, 5].

Methods of Interest

In this work only a few of the many methods of NDT will be investigated. This work is aimed to shed light onto some of the methods that are currently being used or methods that have shown great promise in the fields of aerospace or power generation. These enviroments are very extreme as they often contain hot temperatures, aggressive airflows, and heavy cyclic loading. The methods that are to be used to gather data from a given system, such as a power generation turbine, must be both fast and accurate. The speed and accuracy of the method of NDT will ultimatly increase the efficiency at which the system is able to run. Components that are used in a power generation turbines, must be inspected while the machine is offline in a quick and efficient manner. The right method must be selected for this particular task. Some of the methods that will be analyzed and experimented with for this work are acoustic thermography, laser acoustic thermography, and photoluminscence piezospectroscopy. Some experimentation has been performed that helps to investigate the mechanics of how this methods of NDT are completed and how to better increase the resolution of these methods. Another aspect of this work is the utilization of computational numerical modeling to help to describe the mechanics of some of these NDT measurement techniques.

The ultimate goal of NDT is to obtain all possible relevant information to the operation of a system. Because this is the goal, the ability to replicate a method using computational numerical modeling is critical for the completion of this task. A word often tossed around industry which describe this goal is the digital twin. It is well known that the possession of a digital twin will give both a better understanding and a higher operational efficiency for a given system. To summarize, digital twin technology will inevitably contribute to both our understanding of the physical sciences, as well as our ability to manipulate them.

CHAPTER 2: ACOUSTIC THERMOGRAPHY

Background

Acoustic thermography is a NDE method where a physical excitation signal is transmitted into an engineering component and its effects are measured using instrumented setups [6]. Typically, the ultrasonic elastic waves generated by the acoustic source will give rise to a thermal anomaly when interacting with a defect (or flaw) such as a crack in the material through the physics of wave-defect interaction. It is generally agreed that for metalloids heat is induced in the defects via frictional rubbing of the crack asperities and plasticity heat at the crack tips [7, 8, 9].

The thermographic principle of using heat generation for measurement has recently been shown to be of tremendous technological importance for IR based turbomachinery and high performance structural health monitoring which can benefit turbomachinery management and maintenance [10, 11, 12, 13].

To elicit an ultrasonic wave into the component of interest, the horn of an ultrasonic welder is placed in contact with sample and directly inputs the signal via force. Another feasible method of ultrasonic wave generation is via piezoelectric transducer. Because the ultrasonic welder is capable of higher amplitudes, it was selected as the method of inducing the ultrasonic waves into the component of interest. Frequency modulation has also shown to have a positive effect on heat generation and defect detection [14, 15, 16]. Frequency modulation is typically only used with piezoelectric transducers, however a device has been developed that affords this ability to ultrasonic welders [17]. For the purposes of this paper the frequency of the signal will remain constant. Acoustic thermography has proven to be more effective than other forms of thermography, due to the ability to detect subsurface cracks [18]. Acoustic thermography is capable of not only detection, but also identification of cracks or defects. Reference systems for flaw detections

were developed by Zombo et al. [19] to define the relationship between measured thermographic signals and the defects they represent. Acoustic thermography is of tremendous importance to health monitoring of turbomachinery because of its ability to detect defects in situ. This technique provides higher detectability and is less invasive than other ultrasonic techniques and other thermographic techniques.

Of the myriad types of defects, cracks are of special significance since they can result in catastrophic failure of the components. In order to design and maintain systems that can non-invasively detect cracks both rapidly and reliably, a systematic study is necessary to understand the various physical factors which correlate with a good thermographic signature. Several well-known challenges remain in advancing in this direction from both a modeling perspective as well as experimental considerations. For instance, from the experimental side it is often difficult to fabricate at lab scale samples which are faithful to the full extent of the complex geometries like turbine blades. Similarly, generating an experimental crack which is close to a true crack is not trivial. It is critical to generate defects which are as close to true cracks as possible and not merely manufactured notches to imitate the conditions that give rise to the thermo-mechanical physics which generates the thermographic signatures. At the same time a high sensitivity infra-red camera (IR camera) is required to detect even the faintest of the signatures from the area of analysis to compare with parametric studies of the computational counterparts.

From the simulation perspective, the computational challenges are often no less daunting. The very complexity of a blade geometry puts a massive load on both pre and post processing of any finite element (FE) solver. More problems arise due to possible nonlinear effects of contact or localized plasticity of the material. Similarly crack face contact interactions most certainly call for advanced commercial FE solvers. If more information is sought such as extensive parameter analysis or long term elasto-dynamic response, even a workstation computer may not be sufficient. FEA, if used effectively, is a revolutionary tool to study and replicate the behavior of ultrasound in a solid media, and the effect ultrasound has on material defects [20, 21, 22, 23]. This includes

investigating the dimensional effects of a defect with the amount of heat generated [24].

There has been an abundance of experimental research performed on generic block samples with manufactured defects, rather than using complex geometries found in industry with authentically formed flaws. In this study we examine turbine blades with cracks formed during operation of turbomachinery as well as artificially manufactured authentic cracks. Thus our results are aimed to be more in line with the actual operating machinery than only lab scale specimens. The manufactured crack under consideration in this paper was circumferential and was fabricated utilizing the cold pin insertion technique.

A FE model was developed using commercially available FE software ABAQUS (Dassault Systemes) on a reduced geometric model to study the crack-wave interaction physics. Validating and evaluating this model on a known acoustic thermographic technique will allow us to use it for a model based evaluation of newer more advanced pulsed based NDT discussed later. Furthermore, fostering a deeper understanding of the various factors will also allow us to optimize such a method for obtaining better thermographic signature and also delineate the limits of performance.

To this end, in this paper, we develop a model and systematically probe the effect of crack geometry, localized plasticity, and frictional effects in generating the thermographic signature for an acoustic experiment with an ultrasonic welder. After isolating these factors, we simulate a pulse loading technique to evaluate its model based performance.

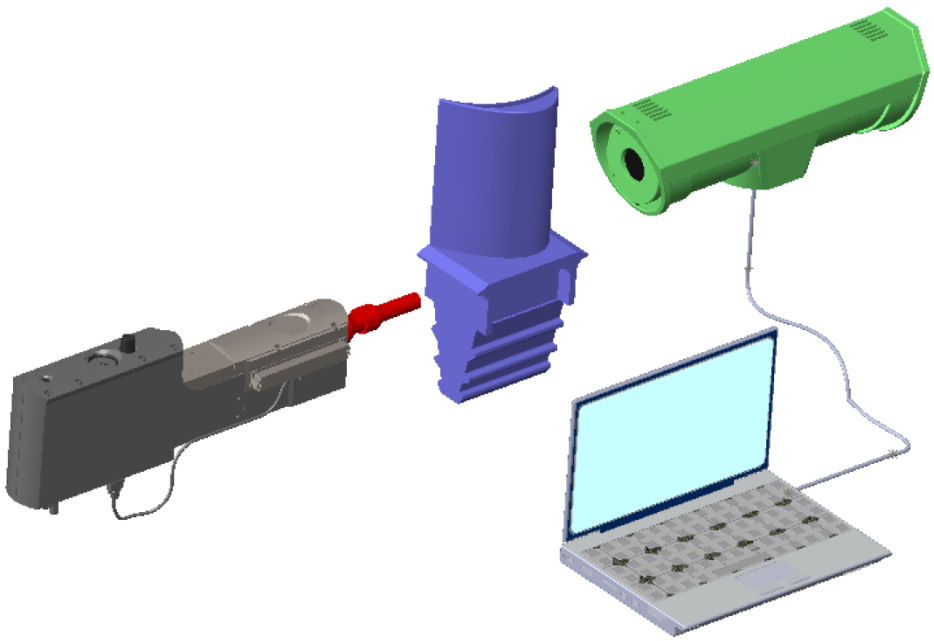

Figure 2.1: Schematic of experimental setup of the acoustic thermographic nondestructive testing procedure. This includes the ultrasonic welder, turbine blade, infrared camera, and computer

Experimentation

The experiment conducted consisted of testing of three gas turbine blades with cracks, as shown in Figure 2.1. The ultrasonic welder made repeated rapid contact at the root of the blade which caused elastic waves to emanate from the source and radiate throughout the turbine blade. This contact occured at the base of the turbine blade. The ultrasonic waves generated inside and throughout the turbine blade then interacted with the flaw to produce a thermal signature which was measured using a highly sensitive IR camera. The signals were then transferred, stored, and displayed on a computer.

We used three different turbine blade samples each with a distinct type of crack. The pictures of the three cracks are shown in Figures 2.2, 2.3, and 2.4. For the first two of the blades, the cracks were a result of an actual operation in a gas turbine. The crack lengths were measured to be 0.5cm and 4cm respectively. The third blade had an artificially created circumferential crack using a cold pin insertion with a diameter of 2.5mm. A cold pin insertion crack was formed by drilling a hole in the turbine blade, and creating a cylindrical pin of the exact same size. The pin would not fit in the hole initially at room temperature. However, when the temperature of both the pin and blade were lowered enough to cause sufficient contraction, the pin could be inserted into the hole. When the blade and pin return to room temperature the pin now fits tight against the drilled hole in the turbine simulating an actual crack.

All of the blades received a physical excitation from the ultrasonic welder. The ultrasonic welder used for this experiment was a Branson X2000. A frequency of 20 kHz was used to propagate ultrasonic waves into the turbine blades using this ultrasonic welder. The physical excitation occurred for a total of one second. The thermal signature of the defective area was observed using an IR camera (FLIR SC8200) with frame rate of 132 Hz. The thermal profile of the area of interest was recorded during and after the physical excitation of the sample. This is a full field camera which gives measurements in greyscale counts which roughly correlate with temperature rise. However, exact temperature measurements are very difficult to obtain from this signature. To augment these measurements, we also used another FLIR E50 camera to measure point temperature at the crack region. This gave us an estimate to be used for comparing with our FE model. This camera measured temperature rise in degrees Celsius. We found that the temperature rise was linear with time for all cases. This allows us to run FE simulations for much smaller duration of time and then linearly extrapolate saving computing time.

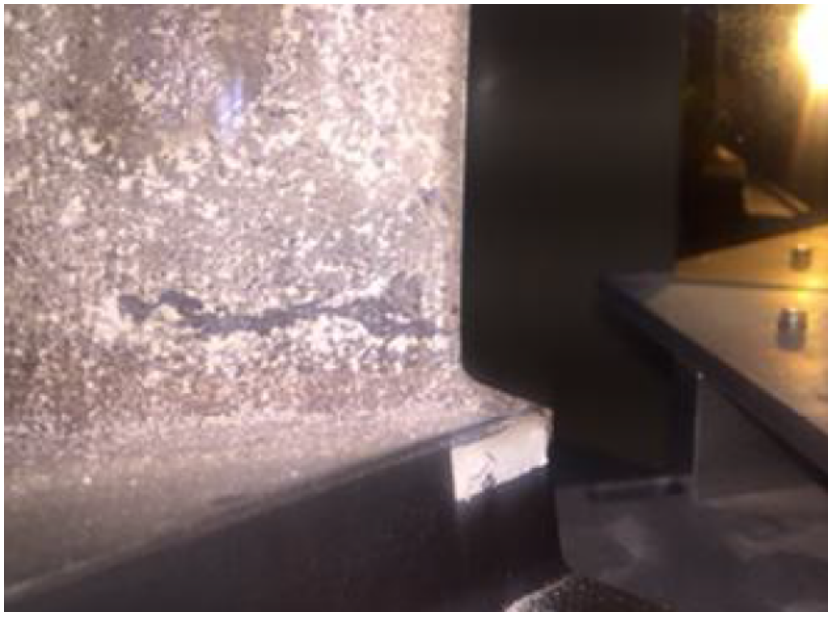

Figure 2.2: Turbine blade with a 4 inch crack which was caused from operation in the field

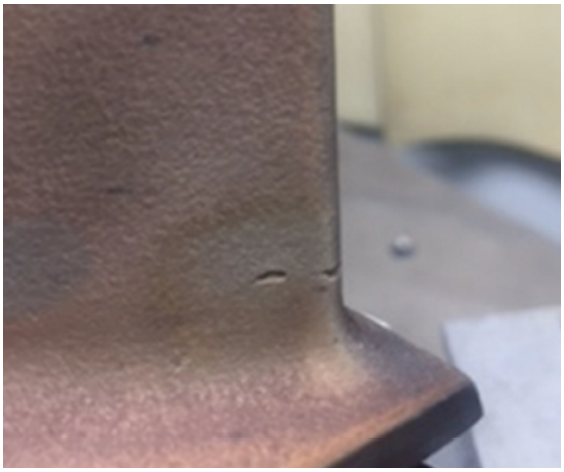

Figure 2.3: Turbine blade with a 0.5 inch crack which was caused from operation in the field

Figure 2.4: Turbine blade with a pin crack (circular). This crack is a manufactured crack for experimental purposes

All of the blades received a physical excitation from the ultrasonic welder. The ultrasonic welder used for this experiment was a Branson X2000. A frequency of 20 kHz was used to propagate ultrasonic waves into the turbine blades using this ultrasonic welder. The physical excitation occurred for a total of one second. The thermal signature of the defective area was observed using an IR camera (FLIR SC8200) with frame rate of 132 Hz. The thermal profile of the area of interest was recorded during and after the physical excitation of the sample. This is a full field camera which gives measurements in greyscale counts which roughly correlate with temperature rise. However, exact temperature measurements are very difficult to obtain from this signature. To augment these measurements, we also used another FLIR E50 camera to measure point temperature at the crack region. This gave us an estimate to be used for comparing with our FE model. This camera measured temperature rise in degrees Celsius. We found that the temperature rise was linear with time for all cases. This allows us to run FE simulations for much smaller duration of time and then

linearly extrapolate saving computing time.

Finite Element Analysis

A FE analysis was conducted on these three types of defects using a commercially available FE software ABAQUS (Dassault Systemes) [25]. This method is very effective for probing the behavior of ultrasonic waves in solid media, and for predicting the heat that could be either frictionally generated via the asperities of the crack or due to plastic work at regions of high stress concentrations such as crack tip. Note that the FE model does not have to consider the entire complex geometry of the turbine blade since the duration of the event, the remote location of the acoustic radiation source and amplitude of excitation do not warrant boundary effects from the actual turbine for this particular set of simulations. The remote strain due to displacement load is simply transferred to the boundary region.

Therefore, only the area near the near vicinity of crack was meshed and analyzed rather than the entire turbine blade as shown in Figure 2.6. Note that scaling down the physical size of sample for the FEA was done maintaining the same boundary strain on the reduced FE model, which caused a reduction in the input signal amplitude proportional to the size of the FE sample.

We used the standard Coulomb friction law to define the frictional contact between the surfaces which is characterized by a single coefficient of sliding friction . A crack was inserted into the FE model using a seam cut. A surface to surface kinematic contact with small surface sliding option was implemented for the opposite crack faces. The heat generated due to this specification was automatically calculated by FE software from the crack surface displacements and imposed contact constraints [26].

The value of friction coefficients and other material properties for Nickel based alloy which is a typical material for turbine blade has been taken from open literature [26, 27]. The material prop-

erties used for the blade material for the analysis are summarized below in Table 2.1. The total time of excitation in previous experimental studies to produce optimal heating results has been one second or less [7, 8, 9]. Recall that the first two crack profiles were formed through actual gas turbine operations. Therefore, the blades were much rougher. The roughness was easy to discern through both touch and visible calcification on the exterior. It is well known that a thin oxide film can raise the coefficient of friction. Such an increase can raise the coefficient of friction from 0.6 to as high as 2.1 for Nickel based alloys [26, 27]. The lowest value of above pristine values due to oxide formation, i.e. 1.2 was used from this study for the initial FE analysis as a conservative estimate. The cold pin insertion resulted in much smoother surfaces as it was artificially created on an unused turbine blade, therefore we used the standard coefficient of friction for pristine nickel-alloy surface, =0.6. Although the actual experiment ran for about 1 second, for the FE analysis the trend line of temperature was recorded for 0.1 seconds and then extrapolated linearly for the rest of the duration till 1 second. This was based on experimental trends and also reduced computation time for the FE computations. Simulations were completed for all three of the crack types shown in Figures 2.2, 2.3, 2.4.

In order to probe the effect of plasticity on thermographic signature, we also carried out simulation with only plasticity of the material as a source of nonlinearity, while neglecting friction. We used plasticity data from material documentation and fitted the best approximation of the plastic behavior. The plasticity parameters used in the model are reported in Figure 2.5. We used the inelastic heat fraction of 0.9 which is common for metal plasticity [26, 27].

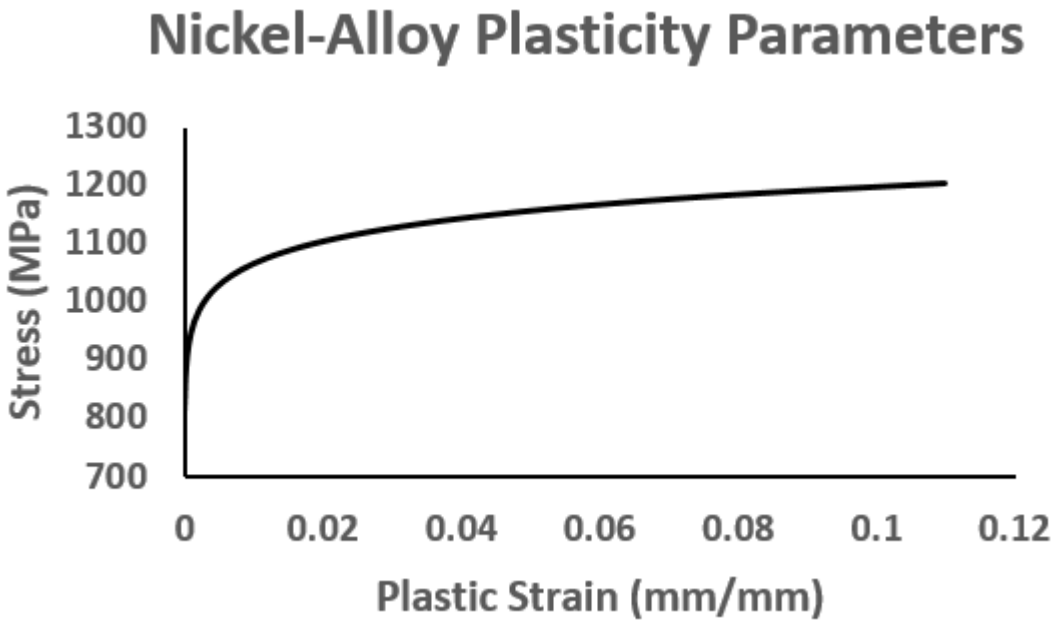

Figure 2.5: Nickel alloy plasticity parameters, a graph of stress (MPa) versus plastic strain (mm/mm)

Table 2.1: Input parameters for Finite Element Simulation

Material Property	**Value**
Coefficient of Friction	0.6 & 1.2
Density	8602 $\frac{kg}{m^3}$
Coefficient of Thermal Expansion	-1.199 x 10^{-5}
Modulus of Elasticity	78.908 GPa
Poissons Ratio	0.31248
Specific Heat	410 $\frac{J}{kg \cdot K}$
Thermal Conductivity	8.4 $\frac{W}{m \cdot K}$

For both plasticity and frictional models, the input signal was 20 kHz, just as the ultrasonic welder used in our experiments. The method of applying the force generated from the ultrasonic welder was a boundary condition of a sinusoidal oscillating displacement equal to the size of the head of the welder. The displacement for this boundary condition was scaled proportional with the size reduction of the total system to maintain similar strains at the model boundary as discussed earlier. The load conditions can be located on the right side image in Figure 2.6. A Y-symmetrical boundary condition was enforced on the two sides of the geometry that are perpendicular to the Y-axis. Note that specific attribution of thermal signature to a particular source is difficult if not impossible to do with direct thermography data. Therefore, computational model can be of special importance in probing the physical origin of the thermal data.

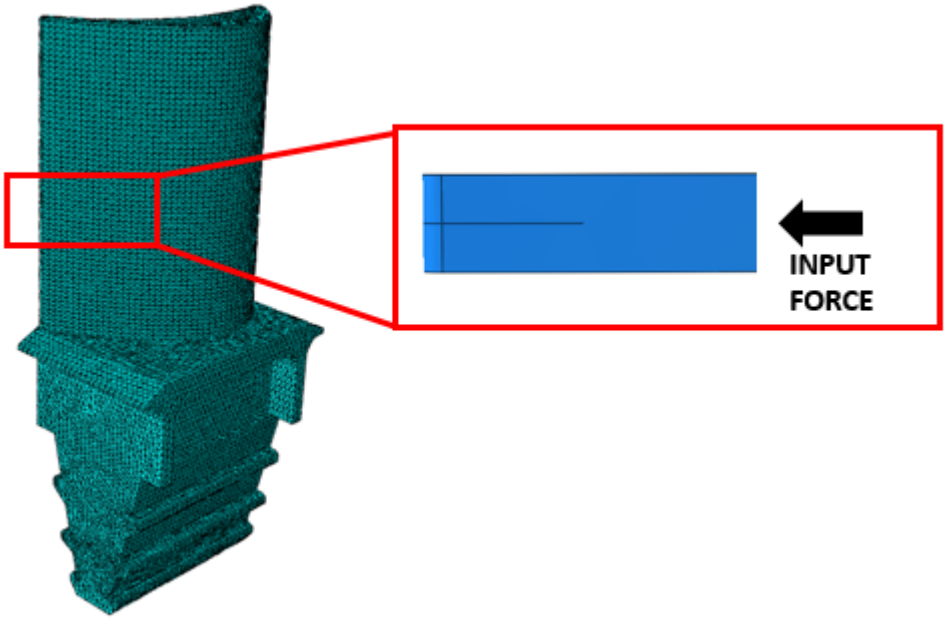

Figure 2.6: Meshed turbine blade reduction, (LEFT) An idealized turbine blade geometry meshed with the location of the crack shown in the red box, (RIGHT) The region of interest for FE analysis showing the area where the force was applied

Experimental and Computational Results

The experimental thermal signature was recorded on all three cracks for a duration three seconds. This includes the one second of excitation and two seconds following the excitation of the turbine blade. We used the FLIR E50 camera to measure the temperature rise at a point. We pointed the camera at the crack vicinity (roughly right on the crack) and measured the maximum temperature rise. All of the results had a maximum temperature after one second of excitation.

We found that the maximum temperature computed by the FEA analysis of the friction-only model was very close to the maximum temperature measured by the FLIR E50 camera. The maximum temperature was calculated from the FE model by taking the average of the points in the immediate area of the maximum temperature contours after FE simulations have run. The maximum temperatures for each of the crack profiles given from the FEA are listed below in Table 2.2.

We also carried out similar calculations from the FE model with plasticity as the source of heat generation, removing friction. Our results conclusively proved that plastic deformation is a negligible source of thermal signature. The results for temperature increase for this case were to the order of 10^{-6} °C or lesser which is negligible. This was true for both edge type cracks as well as the cold-pressed pin crack.

Table 2.2: Experimental and FEA Maximum Temperature Increases

Crack Profile	**Maximum $\triangle$T °C (Experimental)**	**Maximum $\triangle$T °C (FEA)**
2.5 mm Pin Crack	2.4	2.1
0.5 cm Crack	11.1	4.51
4 cm Crack	21.8	8.16

The second source of validation of our model came from comparing the full-field temperature rise profile of our FE model for all three types of cracks, Figures 2.7, 2.8, 2.9. We use the temperature rise as a rough proxy for the count of the IR camera. Using this postulate, we find an excellent match between our FE model and experimental thermal signatures. The results once again showed the dominant role of interfacial friction in thermal signature generation.

Our simulations thus show crack face friction to be the most important contributor to the thermal signature and the success of any new method must rely on maximizing this phenomenon.

Probing deeper into the heat generation field, we find clear differences in temperature rise spatial

distribution in the cracks for different configurations in both experiments and computational models.

One trend that appears to hold is that longer cracks give rise to higher temperature rise. This may seem expected since longer cracks have more surfaces at contact. However, on a deeper look, the picture is more nuanced. For instance, clearly the temperature rise for the 2.5mm pressed fit pin crack was notably lower than the other two types of edge type cracks. However, for this circumferential crack, a 2.5mm diameter gives a crack arc length of about 0.8cm, almost the same order of length as the smaller of the edge crack. Therefore, this drop in temperature was not necessarily due to a lower crack length. The lower temperature rise can be partially attributed to a lower coefficient of friction because the blade with this manufactured cold press-pin crack was unused and uncoated. A second contributing factor to higher temperature rise is the fact that a crack formed through actual operation in the industry is not a completely straight line. The cracks formed through industrial usage tend to be jagged which not only scale up the surface available but also lead to internal strain concentrations leading to larger local displacements. This becomes evident in the V-shaped crack in Figure 2.8 (right side) where more temperature rise occurs near the bend of the crack.

It can be noted that the temperature profile of the 2.5 mm circumferential pin crack was also the closest match to temperature profile of the FEA simulation of this crack. This is caused by the idealness of the pin-pressed crack profile. The crack is uniform in shape (no jagged edges), the coefficient of friction is uniform, and the entire pin is in contact with the hole in the turbine. These ideal conditions are closest to the ideal conditions of an FEA analysis thereby giving us the best match.

It is also important to note that different parts of the crack did heat to different temperatures in both the FEA and experimental observations. This may result in some scatter of results from acoustic thermography.

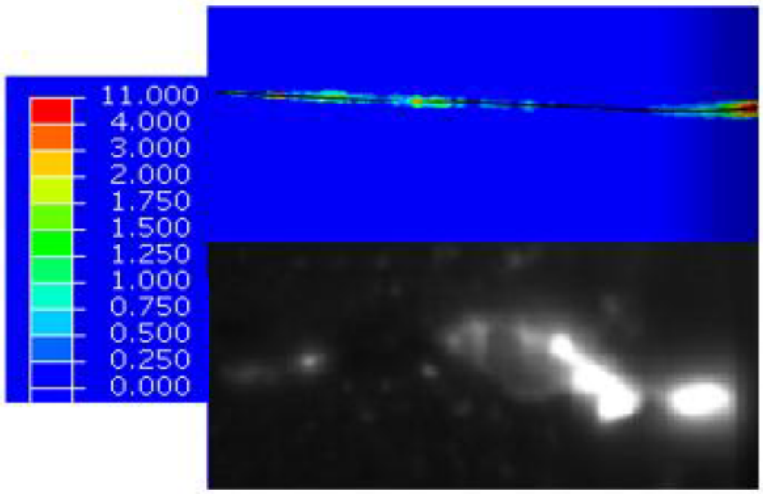

Figure 2.7: Thermal Profile of the Pin Crack, Temperature rise at 0.1 second was linearly extrapolated to 1 second. (LEFT)Temperature Legend °C (TOP MIDDLE) Finite Element Analysis (BOTTOM MIDDLE) Infrared Imaging (RIGHT) Picture of defect with the crack outlined in red

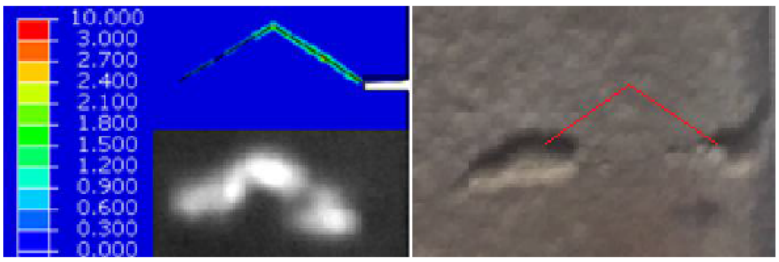

Figure 2.8: Thermal Profile of the 0.5cm Crack, Temperature rise at 0.1 second was linearly extrapolated to 1 second. (LEFT)Temperature Legend °C (MIDDLE) Finite Element Analysis (RIGHT) Infrared Imaging

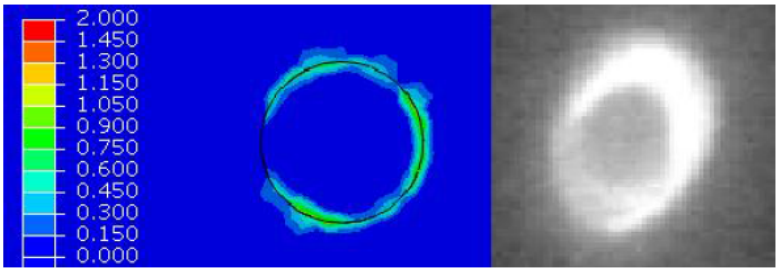

Figure 2.9: Thermal Profile of the 4cm Crack, Temperature rise at 0.1 second was linearly extrapolated to 1 second. (LEFT)Temperature Legend °C (TOP RIGHT) Finite Element Analysis (BOTTOM RIGHT) Infrared Imaging

Discussion/Conclusion

The necessity to monitor the health of components while in operation grows more and more every year. Thermographic acoustic emmision can contribute to real time in-situ health monitoring of turbines. This method has proven the ability to detect both cracks and delaminations. The ability to detect crack and delamintations for any component can contribute to the overall operational efficiency of a manufacuturing process. There are many types of metals which can support ultrasonic waves, and would not suffer any damage from this testing procedure. To be able to detect flaws without damaging components is the main principal of non-destructive testing. Acoustic emmission thermography does have some drawbacks, as it cannot detect sub-surface defects with great reliability. Also it would require some ingenuity to design and implement a system that could test a turbine blade while in operation. This method seems to be more equiped to test a turbine blade in between operational cycles of the turbine.

This study found that a cracked formed through industrial usage will likely have more surface area

due to jagged path and a higher coefficient of friction than an ideal model crack. This is beneficial to the detectability through an acoustic emission technique. This study also found that the main source of heat generation in acoustic emmision is the frictional heat generated in the crack during a physical excitation. Inelastic sources of heat were negligible in this study, and this is the general consesus in this particular field.

CHAPTER 3: LASER INDUCED ACOUSTIC THERMOGRAPHY

Background

The previous part of this paper conclusively established crack surface frictional interaction as the primary source of heat generation. We use the validated values from that section to carry out a model based evaluation of a potential non-contact pulsed based acoustic thermographic technique. This would be unlike the ultrasonic welder which requires a physical contact. However, contact based acoustics also provide a near certain route of delivering the necessary energy required for crack face motion to produce frictional power for heat signatures through the mechanics of contact. In this section, we explore the possibility of a pulsed loading to produce a thermographic signature and report its promise and pitfalls. Such a pulsed loading would ideally produce ultrasonic waves in the material that may have the power and high frequency needed to induce a frictional heating source from either a crack or delamination in a turbine blade. A high powered laser, such as an Nd:YAG laser has been able to produce high powered ultrasonic waves in materials, and has been studied and experimented with since the 1980s [28, 22, 29, 30, 31]. A second trade-off will be an increase in frequency. High powered lasers produce waves to the order of MHz rather than 20-40 kHz waves produced by an ultrasonic welder [31].

Computational Validation

A surface heat flux was used to simulate the laser in the FEA, and the input conditions are listed below in Table 3.1. The penetration depth was set to 0, when in fact depending on the wavelength and properties of the target material, a laser can penetrate up to a few micrometers [31]. This will have some effect on the ultrasonic waves produced via laser, what effect the optical penetration

depth has on the heat generation of defects will remain an open issue. The pulse duration is the time duration of the laser pulse, and the Frequency is the amount of pulses in a second. The pulse diameter is the diameter of the pulse when it comes into contact with the nickel alloy plate shown in Figure 3.1.

Table 3.1: Laser Input Conditions Utilized for Finite Element Analysis

Input Conditions	**Magnitude**
Power	1, 10, 100 (MW)
Pulse Duration	0.5 μs
Penetration Depth	0 m
Frequency	1 (MHz)
Pulse Diameter	1 (mm)
Distance from Crack	1, 5, 8 (cm)

The FEA is even more computationally expensive for the laser input conditions. The step size must be reduced due to the increase in frequency, and it is recommended to increase the mesh density as well. The step size for this FEA was 10^{-8}s and the mesh size was 0.5mm, in order to satisfy the CFL (Courant-Frederich-Lewy) condition, and produce accurate results [32, 33]. A simple block geometry was used in the FEA of this method. This is shown below in Figure 3.1.

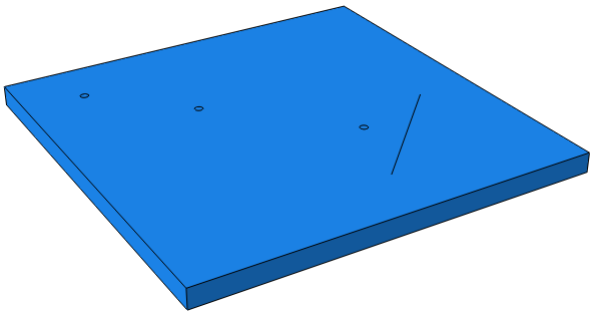

Figure 3.1: Geometry used for the laser simulations, the laser input locations are shown at 1 cm, 5cm, and 8cm from the crack

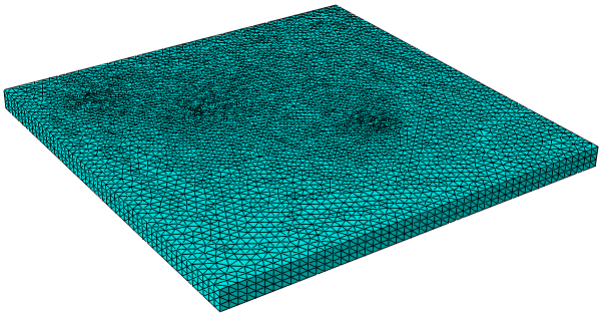

Figure 3.2: The meshed geometry of the laser simulation, showing the mesh density of the simulation

The laser input was modeled as a cylindrical surface heat flux at three different power levels: 1 MW, 10MW, and 100MW, shown in Figure 3.2. Another important aspect of success for this method is how far from the source can the cracks be detected. We placed cracks at three different

distances: 1cm, 5cm, and 8cm. This produced a total of nine different thermal profiles. We used a crack size of 4cm for our numerical simulations. The average temperature for the immediate crack area was taken for each of these analysis. The coefficient friction was taken to be μ=1.2 to mimic a crack from industrial usage. We run the simulation for 0.1s, and then linearly extrapolate the average temperature at 1s. The results are located in Figure 3.3, which plots logarithm of temperature rise $\triangle$T with distance, and we can observe a roughly linear relationship between the two. This translates to the following empirical relationship:

$$\frac{dlog\triangle T}{ds} \approx -k \tag{3.1}$$

In this equation s is the crack distance and k is an empirical constant. Integrating equation 3.1 would yield:

$$log\frac{\triangle T}{\triangle T_0} = -k\left(s - s_0\right) \tag{3.2}$$

In equation 3.3 is the temperature rise at a cutoff distance s_0 and would depend on the Power of the laser. Thus we arrive at the following Beer-Lambert type scaling law for temperature rise and distance, shown in the following equation:

$$\triangle T = \triangle T_0 e^{-k\triangle s} \tag{3.3}$$

Therefore, there is an exponential drop in thermal signature with distance from the laser beam for all powers. However, the decrease is far sharper for lower energy beams since they have a lower pre-multiplying factor $\triangle T_0$. Thus higher energy beams are at a premium. However, what

is interesting to note is that a higher energy beam increases thermal load at the point of beam impingement, increasing the chances of ablation and plastic damage thereby causing destruction of the sample. This is clear from the stress contours seen in the Figure 3.4. These stress profiles show the maximum induced Von Mises stress at the location of beam impingement. Clearly, the maximum stress increases by an order of magnitude with an order of magnitude increase in energy thereby significantly increasing local damage and precipitate ablation if impinged repeatedly or for longer duration.

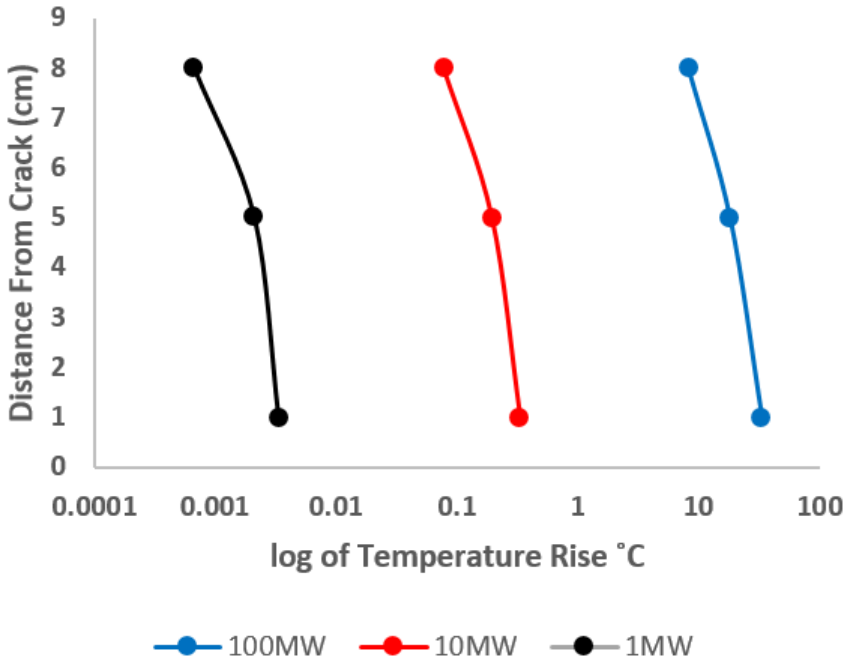

Figure 3.3: Graph of laser heat generation on a logrithmic temperature scale vs distance between excitation signal and defect

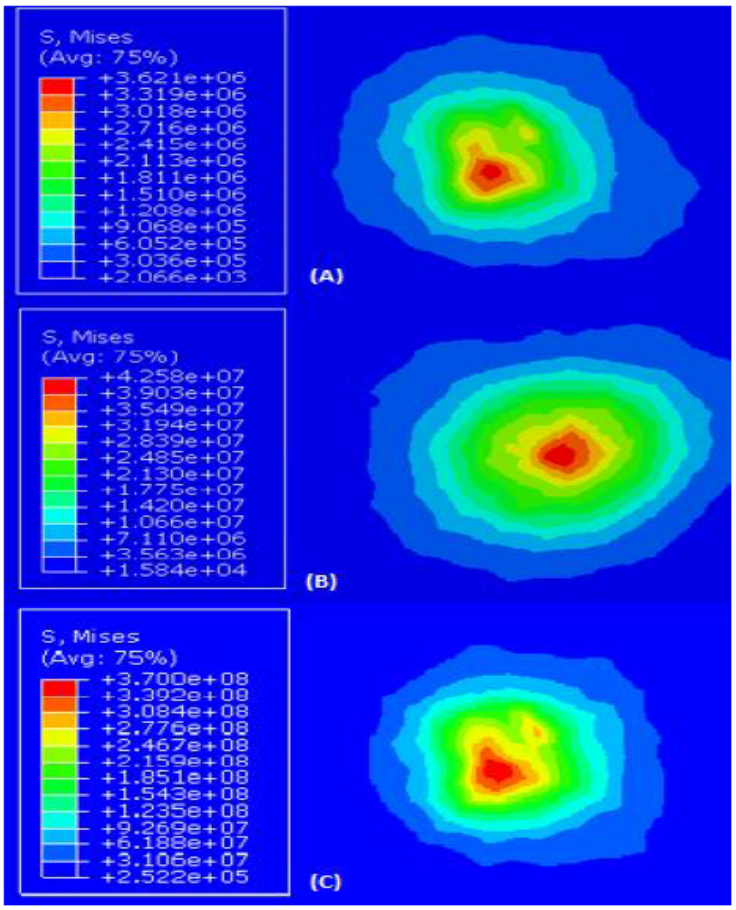

Figure 3.4: Maximum von mises stress profiles in pascals (A) 1 MW (B) 10MW (C) 100MW

Discussion/Conclusion

Laser based acoustic emission techniques can help to fill in the gaps of real time in-situ health monitoring of turbines, by assisting in the detection of defects such as cracks or delaminations. This can be done by utilizing innovative methods of producing ultrasonic waves in materials, a method can be developed that is both non-invasive and non-destructive to the material which is un-

der consideration. Acoustic thermography can be further developed to be a cost efficient method of material examination and increase accurate prognosis for turbomachinery operation. This method has already shown the ability to detect defects which would be undetectable from conventional ultrasonic testing methods, as well as conventional thermographic methods. The cracks detected in this work, both experimentally and through FE simulation further prove the viability of acoustic thermographic technology. The complex geometry of defects formed through turbomachinery operations are particularly opportune for detection through ultrasonic-excited thermography. This paper also evaluated a new method of inducing the ultrasonic thermo-elastic waves into a material. It was demonstrated through FEA that a high powered laser could be implemented for the acoustic input signal for thermographic crack detection but with important caveats. It is clear from this study, and is also generally accepted that friction is the main source of heat generation during a physical excitation of a crack via ultrasonic waves. Frictional heat sources far outwight the heat sources generated via inelastic deformation. A laser could be a viable method of producing ultrasonic waves in a medium that are capable of the excitation of defects to elicit a thermal response detectable through Inferred imaging. A challenge facing this technique is that ultrasonic waves produced via this method will have a more limited amplitude than the waves produced via the physical excitation of an ultrasonic welder. The thermo-elastic waves produced via laser will also have a higher frequency, which will accelerate wave attenuation. Our models indicate that significant challenges exist in replicating the versatility of traditional acoustic thermographic technique for pulsed based laser methods due to a balance needed between thermal signature necessary, signal attenuation from source and possibility of ablation at the point of impingement. Although laser acoustic thermography has not been verified experimentally, this could certainly be feasible in the near future.

CHAPTER 4: STRESS-SENSING ALUMINA NANOPARTICLES

Background

Materials-related drivers for the development of advanced engines include lower weight materials for improved specific fuel consumption; advances in materials that permit innovation in design to achieve improved performance; and reduced materials cost for lower acquisition and maintenance cost [34]. To this aim, composite materials have provided significant gains in performance and weight reduction with their exceptional strength and stiffness-to-weight ratio. The arrangement of high modulus fillers such as alumina, graphite or silica, within matrix materials, offers the potential to selectively enhance mechanical properties such as elastic modulus and fracture toughness and provide for a greater spectrum of selectable material properties. This has led to its expansive use in replacing conventional materials for applications in airframe structures. Improved compressive strength [35] and fracture performance [36] of these materials have been investigated using standard mechanical tests. The general outcomes of improved moduli and strength are largely dependent on the material configuration including the choice of materials, effect of filler volume fraction, particle or filler size and processing. As many of the failure modes initiate at the microscale, research on the mechanisms of composite structural failure and effects of modifying fillers in advanced composites would be greatly enhanced by the ability to map the stress evolution and detect the onset of damage within the materials with high spatial resolution and sensitivity. Fundamental knowledge on the factors governing the mechanisms of load transfer and consequently their strengthening will address what is needed to achieve control and consistency in their mechanical behavior. In this context, alumina particle reinforcement provides us with a unique opportunity to simultaneously enhance strength as well as precisely measure the matrix-particle load transfer characteristic critical for performance prediction using optical spectroscopy. This approach

of utilizing these unique experimental measurements to tune computational finite element models (FEM), creates a powerful tool to elucidate the mechanics of the reinforcing particles and their interactions with the host matrix. Such models, supported with direct empirical load transfer measurements, will accelerate design strategies for reinforced composites. This includes designing ceramic matrix composites through optimizing nanoparticle or nanofiber morphology including size and shape as well as effects of processing parameters, to customize the overall mechanical properties of structural parts relevant for turbomachinery applications.

Experimentally, optical spectroscopy has the potential to fill the voids in the understanding of significant information including strengthening mechanisms and failure initiation in particulate composites that can improve current models. The spectral properties of chromium-doped alumina, a naturally luminescent material, are dominated by two sharp and closely-spaced peaks in the emission spectrum called the R-lines shown in Figure 4.1. The origin of the characteristic R-emission lines is based on optical transitions between excited states and the ground state of Cr^{3+} ions within -alumina. Piezospectroscopy (PS), measures stress-induced shifts of the R-emission lines during laser excitation of the material and this has been characterized as a linear shift represented by $\triangle$v=$\pi_{ij}\sigma_{ij}$ where the wavenumber shift $\triangle$v is related to the stress σ_{ij} through a PS coefficient, π_{ij}. Early research on the stress sensitivity of these peaks citekaplyanskii1962piezospectroscopic, known as the piezospectroscopic effect, led to significant applications to monitor pressure in diamond anvil cells [37] and the method gained importance in the last 2 decades providing life prediction assessments of thermal barrier coatings used on gas turbine engine blades [38, 38] through stress measurement in the thermally grown oxide layer (TGO).

PL imaging concept, PS relationships.

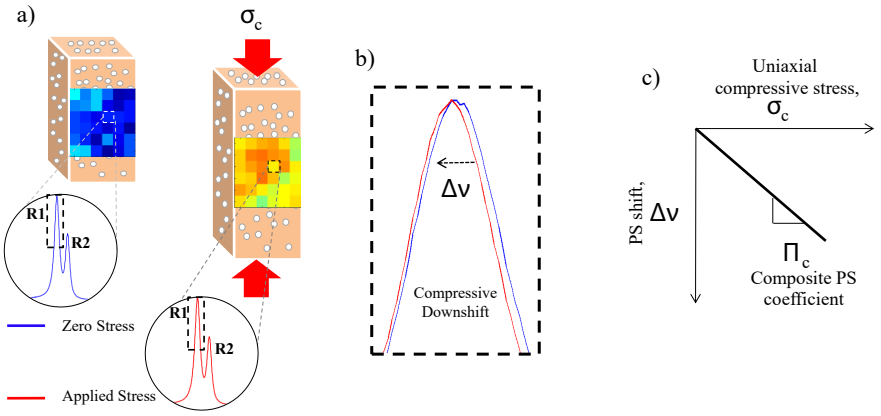

Figure 4.1: (a) A schematic representing hyperspectral imaging of a PS nanocomposite under compressice loading,(b) Diagram of the corresponding peak position downshift under a compressive load, and (c) the composite piezospectroscopic coefficient (π which is the relationship peak position shift and applied stress [33]

Recent work has shown an enhancement of the PS coefficients when the spectrally active material is introduced as nanoparticles into an epoxy system [39]. The PS coefficients have been observed to increase with volume fraction of alumina nanoparticles. The basis of this change in sensitivity is due to the differing rates of load transfer into the inclusions that occurs with varying of their volume fraction. The measurement very uniquely isolates particle response, determining the spectral shifts and consequently the stress distribution only in the particles. Through such measurements

of characteristic optical transitions within the reinforcing particles, micro-cracking and/or micro-plasticity in the composites can be investigated under in situ conditions. The experimental capture of microscale behavior provides an insight into the mechanisms of load transfer that lead to the response under deformation and can even reveal the onset of damage and its progression through measurement of stress release.

In the same way, analytical and simulation studies provide a means to study the effects of different reinforcing parameters. In these simulations the failure of materials are studied through analysis of a representative volume element (RVE), which is defined as the smallest unit cell that can be used to describe the overall composite. The use of an RVE simplifies the geometry of a composite while still maintaining both the particulate and the matrix material properties. Finite element models (FEM) have been developed in recent years that model the effect of debonding on material properties [40] and have been shown to correlate closely with the existing theoretical models. The simulation of particle debonding is used to study the interface effect and shows the importance of particle to matrix adhesion. Although these simulations provide valuable insight to some reinforcement parameters, they are difficult to validate experimentally. Experimental techniques such as piezospectroscopy and X-ray diffraction are unique in their capability to distinguish stresses or strains among individual phases within a composite. The work presented here combines both FE simulation and piezospectroscopy for a basic two-phase alumina-epoxy filler-matrix combination to quantify load transfer in ceramic composites. The findings from this work allow for simulations to be extended for future studies on various parameters such as filler material, size, shape and chemical treatments and how they affect the overall load transfer and mechanical properties of reinforced composites.

Experimentation

The experimental results presented here are based on a series of previously conducted mechanical tests on particulate composites of alumina and epoxy with in-situ piezospectroscopic measurements [39, 41]. The focus of the investigations was to quantify the effect of the volume fraction of -alumina particles, ranging from 5 vol % to 38 vol %, on the piezospectroscopic coefficients. Studies show that minimum 5 vol % particle filler has a positive influence on mechanical properties [42]] whereas the maximum possible vol % that can be achieved while still maintaining uniform dispersion is 43 vol % [43]. Filler particles with an average size of 150 nm were dispersed in an aerospace grade epoxy resin, Epon 862 coupled with Epikure W, serving as the matrix material. The nanocomposites were manufactured as parallelepipeds of dimension 1/8 in. x 1/8 in. cross-section and a length of 1/2 in. with a 4:1 aspect ratio per ASTM D695 [44]. After manufacturing, the samples were tested for density check to confirm the correct volume fraction of the filler particles. A custom portable spectrometer system [45] consisting of a fiber optic probe, 532 nm laser, XYZ stage, and spectrometer was coupled with an MTS Insight electromechanical testing system to collect the photoluminescence data over the surface of the specimens while they were subjected to incremental, uniaxial, compressive loads achieving up to a sample stress of approximately 0.12 GPa. Under a compressive load, the wavelength of the emissions from the dopant material will shift. There are two peak wavelength emissions shown in Figure 4.1. The slope of the two plots of peakshift with stress of the characteristic R-lines provide the particulate composite piezospectroscopic coefficient, c which relates the composite stress c, established from the externally applied load to the composite sample, to the measured peakshift through $\triangle_c = \Pi_c \sigma_c$. For this particular dopant there are two peak wavelengths emitted, therefore c can be represented by R1 for the first peak and R2 for the second. The spectral shifts of the photo-luminescent (PL) R-lines for polycrystalline alumina poly have been previously correlated in literature to the hydrostatic stress $(1/3)\sigma_{ii}$ by the PS coefficient Π_{ii} [46]. For the stress sensitive peaks, Π_{ii} has a value of

7.59 $\frac{cm^{-1}}{GPa}$ and 7.62 $\frac{cm^{-1}}{GPa}$ for R1 and R2 in polycrystalline alumina respectively. Considering that the nanoparticle reinforcements are under hydrostatic stress, the peakshifts of the polycrystal and the particle can be equated so the ratio $\frac{\Pi_c}{\Pi_{ii}}$ provides the stress ratio of the hydrostatic to composite stress known as the stress ratio.

$$\frac{\frac{1}{3}\sigma_{ii}}{\sigma_c} = \frac{\Pi_c}{\Pi_{ii}} \tag{4.1}$$

This ratio in equation 4.1 can be determined from the experimental results and used to represent the experimental load transfer for each volume fraction case.

Table 4.1 shows the PS coefficients [39, 47]. and corresponding stress ratio from the previously described experiments in the experimental section. Experimental measurements of peakshifts of photoluminescent emissions isolate the response from the alumina filler particulates to show that with increasing volume fraction of PS particulate filler, the sensitivity of the PS effect, as seen in the PS coefficient c, increases. The corresponding stress ratio increases with a steady but small slope up to about 25 vol % of filler and past this, a sharp increase in stress ratio is observed for the 34 vol % and 38 vol % alumina composites.

Table 4.1: Experimentally determined piezoscpectroscopic coefficients and calculated stress ratio

Volume Fraction	**PS Coefficient R1** $\frac{cm^{-1}}{GPa}$	**PS Coefficient R2** $\frac{cm^{-1}}{GPa}$	**Stress Ratio** $\frac{\Pi_c}{\Pi_{ii}}$
5%	-3.16	-2.60	0.416
20%	-3.34	-3.19	0.44
25%	-3.65	-3.42	0.481
34%	-4.10	-3.88	0.54
38%	-5.63	-5.08	0.742

Figure 4.2 below displays the stress ratio plotted along with theoretical values of the stress ratio quantity obtained from the Eshelby method. The comparison shows that although the Eshelby model predicts the stress ratio reasonably at smaller volume fractions, the trend from the experimental data is distinctly different from theory.

The experimental and Eshelby theory results do show some agreement, but the trend lines diverge at higher volume fractions. At low loads and/or low volume fractions, the particles are expected to be under hydrostatic stress conditions. At higher loads and/or high volume fractions, Hertzian theory defines the stress due to inter-particle contact [48], which becomes the dominant mechanism. The clear anomaly in the PS signature of the alumina nanocomposite with increased concentration of nanoparticles cannot be explained from existing models without unrealistic extrapolation of physical and geometric parameters.

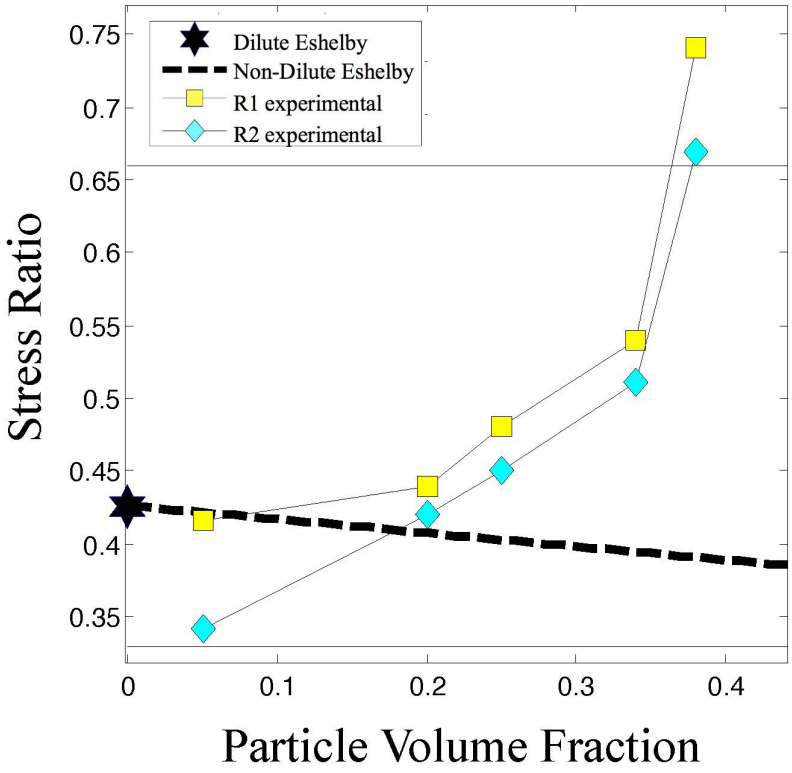

Figure 4.2: Volume fraction plotted againts the R1 and R2 stress ratio (calculated from experimental data) and the theoretical Eshelby model [24]

Computational Methods Initial Investigations

In this study, we explored the postulate of inter-particle contact (or near contact) as the causative phenomena using finite element (FE) simulations. In order to understand this in greater detail, we carry out our first FE analysis (FEA) which simulated the effects of a varied inter-particle distance between two alumina nanoparticles. The inter-particle distance is defined as the distance between the centers minus the diameter of two alumina nanoparticles in the simulation. The effect

of inter-particle distance on the pressure distribution is shown in FE contour plots in Figure 4.3. Rather than selecting arbitrary distances between particles, the distance was normalized by setting the inter-particle distance to a percentage of the radius, R. For this simulation, both the spherical particles were of equal sizes. The inter-particle distance was initially set to zero (contact), and then increased by intervals of 0.1R. The intervals continued until reaching R which was sufficient to resemble no contact/material constriction condition. The simulations were carried out for three of the volume fractions that were tested experimentally for comparison purpose (5%, 25%, and 38% vol).

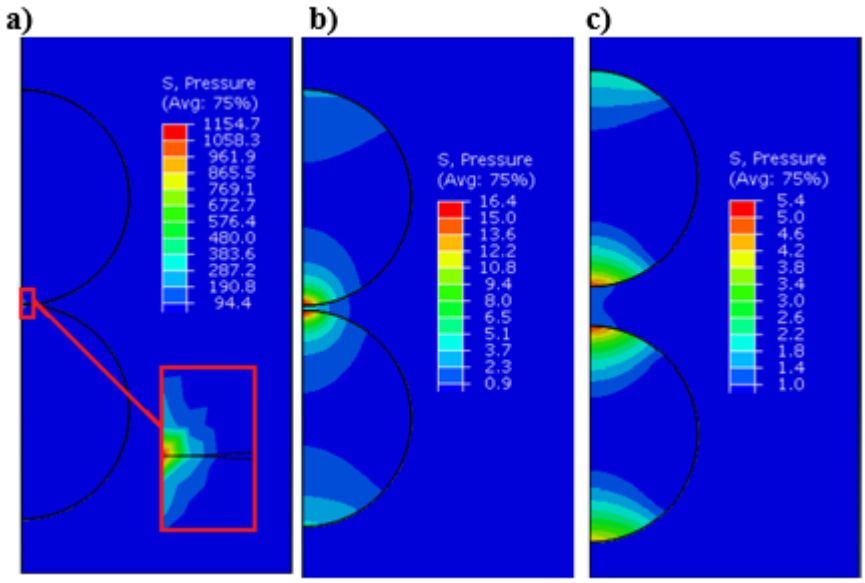

Figure 4.3: Pressure profiles (non-dimensionalized by applied pressure of 1Pa) for a volume fraction of 25% (a) Inter-particle distance = 0%R = contact (b) Inter-particle distance = 10%R (c) Inter-particle distance = 80%R (note: R = radius of the sphere used in simulation

The stress ratio (defined in Eq. 4.1) is used to relate the stress of a particle directly measured

via piezospectroscopic experimentation and the theoretical models produced through FEA. Figure 4.4 shows the effect of contact as well as the effect of minimal distances between nanoparticles on the stress ratio. There is a sharp increase in the stress ratio for all volume fractions when the two particles come closer than 0.1 inter-particle distance continuing to increase until actual contact is achieved. For nanocomposite with a higher volume fractions of alumina, there is a greater probability of these alumina nanoparticles to contact or at least come closer into the vicinity of one another. This FEA demonstrated that contact between particles or even limited distances between particles can increase the induced stress of these particles. Therefore, we strongly believe, that the increases in the stress concentration from the experimental data in higher volume fractions could be caused by contact or near contact conditions between the alumina nanoparticles.

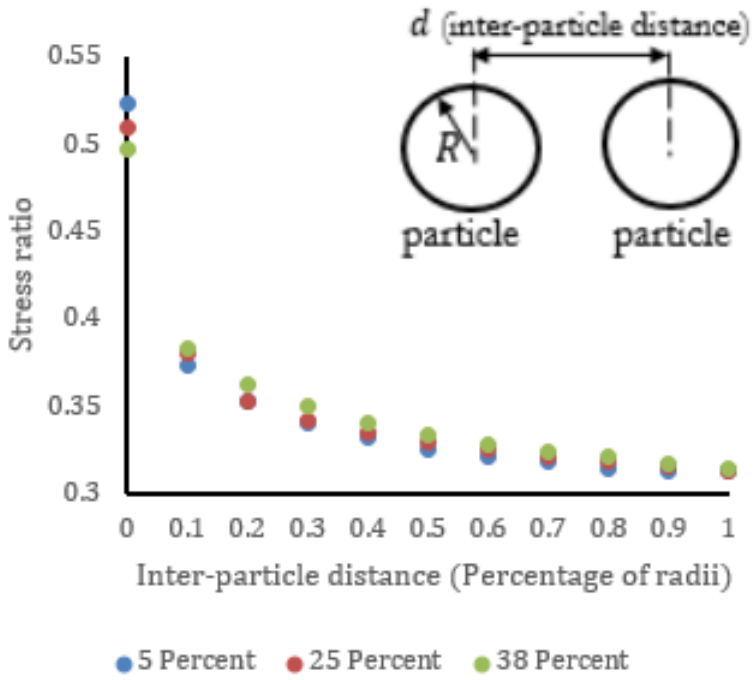

Figure 4.4: Inter-particle distance plotted against stress ratio using FE simulations on geometry shown in the schematic in the upper right of the graph. These simulations were completed for 5%, 25%, and 38% volume fractions

The second FEA will delve into this contact between the nanoparticles and examine the relationship between the radii of the nanoparticles in contact. The larger of the radii in contact will be divided by the smaller of the radii in contact to create the non-dimensionalized radius ratio. The following simulation examined the stress profiles generated by radius ratios from 1 to 5. The radius ratio can be more clearly understood in Figure 4.5, which shows 2 of the 5 different radius ratio layouts for the FEA.

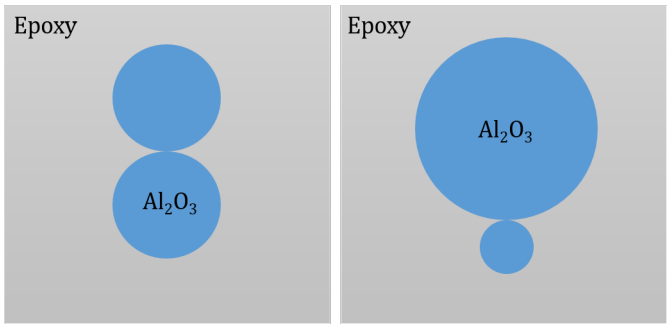

Figure 4.5: Schematic illustration of alumina particle contacts. The circles are the two-dimensional representation of spheres of different sizes (a) 1/1 Ratio (b) 3/1 Ratio

Theoretically, the simplest type of contact, assuming only linear elasticity is well known and the subject of Hertz contact theory [48, 49]. The Hertz theory predicts that local stresses would depend on both the material properties of the bodies in contact as well as the relative contacting profile of the bodies typically quantified by their local radii of curvature. For our current problem, we study the effect of various radii of curvature of particles in affecting the stress ratio for various volume fraction of particles. In order to carry out these simulations, we held the volume fractions constant at 5%, 25%, and 38%. The top side had a pressure of 1 kPa applied and the bottom had a boundary condition of fixed vertical displacement. The left side was axisymmetric, while the right side was free. The radius ratios of 1 through 5 were carried for each of the volume fractions. The alumina particles experienced direct contact with one another in each of the simulations, as the inter-particle distance was held constant at 0 for these simulations. The stress ratios for contrasting radius ratios can be viewed below in Figure 4.6.

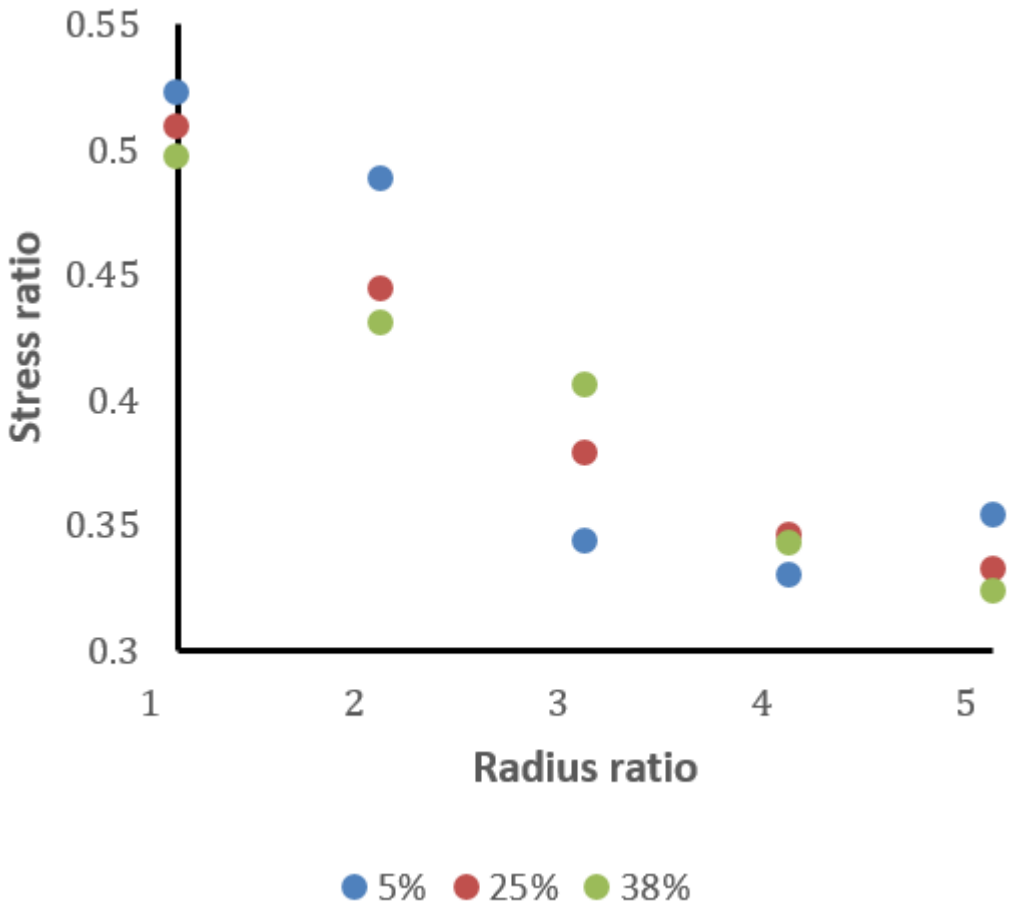

Figure 4.6: Radius ratio plotted against the stress ratio (geometry for simulation is in Figure 4.5)

This simulation shows that stress ratio typically falls as the contrast between the radius of contacting particles increases. This fall is consistent across volume fractions. A typical source of wide range of variation of radius of curvature could be due to manufacturing defects. Our results show that maximum stress ratio is obtained when radii of the particles are similar. This explains the consistent observation of the anomaly since drastic manufacturing defects for nanoparticles are

typically not widespread. In our final FEA we delved even deeper in the effects of contact between the alumina particles on the stress ratio. For this analysis, the number inter-nanoparticle contacts vs. the amount of stress generated in the alumina was evaluated. A 1.25 x 0.8 epoxy block was used for this simulation to allow room for the nanoparticles to achieve contact in a vertical alignment. The number of contacts will be evaluated in the range of 0 to 4 contacts. The layout of the model with two locations of direct contact can be seen in Figure 4.8. The right side shows the boundary conditions, which are a 1 kPa pressure applied to the top surface and a fixed vertical displacement for the bottom surface. The middle image shows the 0.01m mesh utilized for this study; this is the same as the previous two FEA. The image on the far right illustrates the pressure profile. The number of contacts were varied for this model by altering the number of particles as well as the radii of said particles, in order to satisfy leaving the volume fraction constant at 25%.

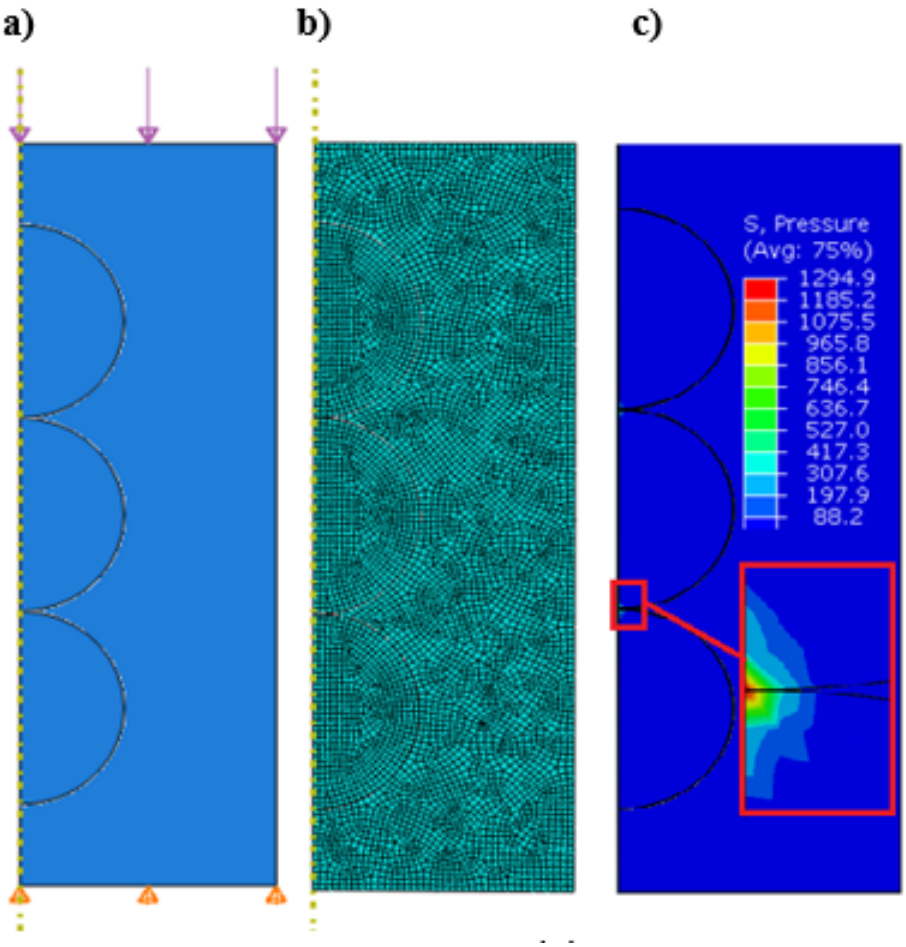

Figure 4.7: Inter-nanoparticle contact FEA (a) Boundary conditions (b) Meshed axisymmetric model (c) Von Mises stress profile (non-dimensionalized by applied pressure of 1Pa)

Note that although contact even at dilute concentrations shows a sharp increase in the stress ratio that is not evident in the experimental spectral diagram (Figure 4.2). This is primarily due to a smaller probability of contact at lower concentration. Similarly, we notice that at higher concentrations the PS continues to increase although our FE calculations indicate near convergence. This

is because, as concentration increases, the probability of multiple contacts also increases, which further increases the stress ratio. We capture this phenomena using a plot of stress ratio for multiple contacts at various concentrations Figure 4.8. We went beyond the stress ratios needed to match the experimental results, this was only to show the pattern, which is, as the number of contacts increases so does the stress ratio. If the volume fraction were to increase, the probability of inter-particle contacts would inevitably follow this same trend [49]. The experimental stress ratio data in Figure 4.2 shows a sharp increase as the volume fraction of the additive material (alumina) is increased. The inter-nanoparticle contact FEA simulations show a similar trend as the number of contacts are increased. The combination of these results points to the conclusion that, higher stress ratio seen at higher volume fractions in the experimental data could have been caused by an increase inter-nanoparticle contacts in the sample. From this study, the experimental and simulation results are in agreement. At low loads and/or low volume fractions, the particles are expected to be under hydrostatic stress conditions. At higher loads and/or high volume fractions, Hertzian Contact theory defines the stress due to inter-particle contact [50], which becomes the dominant mechanism which is taken care of in our FE model.

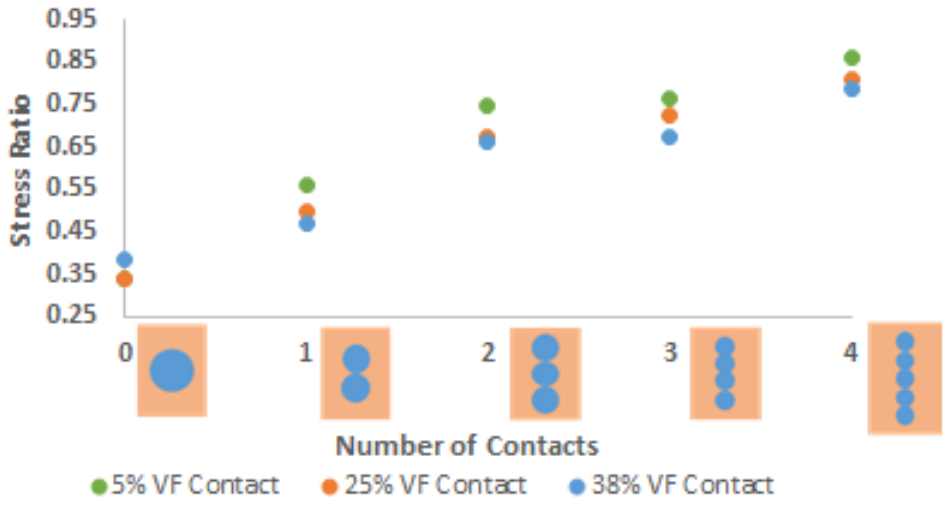

Figure 4.8: Inter-nanoparticle contacts vs. Stress ratio at 5%, 25%, and 38% volume fractions

The additive material used in this experimental work and the FEA was alumina. Alumina has also been shown to have a positive effect on the oxidation rate hot corrosion resistance of YSZ (Yttria-stabilized zirconia). By doping YSZ with alumina, experiments have demonstrated a reduction in the formation of TGO (Thermally Grown Oxide) for the thermal barrier coating (TBC) [51, 52, 53]. Just as the stress ratio can be determined via piezospectroscopic measurement techniques, the modulus of elasticity and other material properties can be determined as well. This is just one industry that could benefit from a better understanding of nanoparticulate composite mechanics.

Discussion/Conclusion

Results of this study from the experimental results and the FE analysis allow an insight into the micromechanics of filler load transfer in ceramic reinforced composites. Results from previous piezospectroscopic experimental works have demonstrated the high stress ratios in nanocomposite materials where alumina volume fractions exceed a volume fraction of 25%. This phenomenon could not be explained by traditional inclusion micro-mechanics from classical elasticity theory which describe stress levels of embedded inclusions in composites. The FEA in this study has shown that the most probable cause of this anomaly to be the inter-particle contact of the embedded alumina nanoparticles in the epoxy matrix. An increase in the number of nanoparticle contacts directly correlates to an increase induced stress levels alumina, which trigger the piezospectroscopic wavelength shift from the previous experimental evidence. An increase in the volume fraction, increases the probability of contact between the nanoparticles, hence the increase in the stress ratio as the volume fraction exceeds 25% alumina. A better understanding of nanoparticulate composites could help contribute to the broad range of industries which have use for this material. The ability to extract data from nanocomposites which utilize particles will ultimately result in an increase in health monitoring efficiency for the industries which they are compatible with such as aerospace or turbomachinery.

CHAPTER 5: PROBABILISTIC LOAD TRANSFER FOR NANOPARTICULATE COMPOSITES

Introduction

Piezospectroscopy (PS) measurement techniques yield the ability to directly measure the amount of stress generated within the nanoparticles for composites under an applied load. Current predictive techniques at higher volume fractions of embedded nanoparticles fail to accurately describe the percentage of load that should be transferred to the nanoparticles while the composite experiences an applied load. Determination of the elastic modulus and other material properties is possible from the PS response of a material at low volume fractions of an embedded ”smart” nanoparticles. The goal of this work is to improve predictive techniques used on nanoparticulate composites with higher volume fractions of nanoparticles. This will be completed by implementing a term for inter-particle contact into current predictive techniques, and also have this term weighted by the probability of contact occurrence. For this study the host material will be an aerospace grade epoxy and the particulate material is alumina, however the techniques presented in this paper could be applied to many different particulate composites. The implications of this work will bring a better understanding of the inter-particle behavior, load transfer theory, and predictive techniques that are currently characterizing the field of nanocomposites.

Nanoparticulate composites are finding uses in several fields, and have received significant attention. One area that has proven quite interesting is the utilization of piezo-spectrospic measurement techniques to determine material conditions, and even material properties. If a matrix mate-rial is doped with a nanomaterial capable of creating spec-tral emission shifts, such as alumina, the composite will gain the ability to sense stresses within [54, 55, 56]. Being able to measure the stress endured by the particles of a specific nano particulate composite could provide greater insight into

the mechanics and understanding of this field in gen-eral. These piezospectropic measurement techniques will increase efficiency in many fields. Aircraft grade epoxies could be doped with photo luminescent materials to pro-vide faster feedback of the condition of the composite material, as well as the material the epoxy is applied to [39]. Another area where this technique could see industrial ap-plications thrive is on TBC coatings of turbine blades for both aircraft and power generation [51].

At low volume fractions ($\phi \leq 20\%$) of the filler material, the predictive techniques prove to be adequate. Currently predictive techniques have demonstrated the ability to de-termine the percentage of load the will be transferred to the filler material, but only at lower volume fractions. The de-termination of the mechanical properties of the material, such as the modulus of elasticity, can currently be accu-rately at lower volume fractions as well. A few examples of these mechanical property predictive techniques are the Mori-Tanaka, Hashin-Stickman, Kim, and Diluted Eshelby. It should be noted the thermal properties also suffer from greater inaccuracy in predictive techniques at higher volume fractions. Piezospectroscopic measurements can contribute to the field of Nanomechanics and improve the predictive techniques at higher volume fractions for nanoparticulate composites.

This study will aim to improve the currently used predictive techniques at higher volume fractions. This will be accomplished by introducing an analytical solution which contains a probabilistic weighted value for inter-particle contact into the equation. A probability will also be introduced to account for the angle of contact. There is good agreement in the field that inter-particle contact at higher volume fractions does contribute to some of the inaccuracies of the previously mentioned predictive models. Inter-particle contact can be broken down into two parts. The first part is the calculation of the stress generated from the particles in contact, and angle of contact is a factor in this equation. The second part would be the quantification of the probability of contact, and to build further off of that, the probability of the occurrence of multiple contacts to any given particle. RVEs (representative volume elements) could use these probabilities to more accurately predict

the load transfer and material properties of a given particulate composite.

A compressive load applied to Cr^{3+} doped polycrystalline alumina has been previously demonstrated to cause a decrease in the wavelength emitted after excitation via laser [46, 57]. This material can be combined with an epoxy to form a nanoparticulate composite capable of sensing the stresses within the alumina. This phenomena was manipulated to measure the stress of the alumina while simultaneously applying a compressive load P to the composite material. This process was completed for 5 different volume fractions seen in Table 4.1.

Probabilistic Spherical Dispersion Description

This predictive technique proposed in this paper includes a term for the probability of contact and a probability of multiple contacts. A set of probabilistic equations on spherical distributions were derived by Torquato [49, 58, 59, 60]. These "nearest neighbor functions" can determine the probability that a spherical particle is within a certain distance from another spherical particle. If the reader is interested in the workings of these probability functions please refer to the sources, as a description of the governing equations can be quite lengthy and is unnecessary for this work. Below in Figure 5.1 is a map derived from the "nearest neighbor functions". The map on the right is to show the particle at the center in red with incremental spaced regions in a variety of colors, each of which represents a distance away from the particle. The distances are increased in increments equivalent to a percentage of the radius of the particle. Calculations were carried out for a range of 0% to 50% volume concentration of the spherical particulate filler material, however Figure 5.1 only lists 5%, 25%, and 38% volume fractions. This is to give the reader a sense of the behavior of the probabilities for some of the volume fractions which were used in the experimental analysis. The percentages in the table on the right represent the probability that another particle will lie within the region. This chart tells us what common sense could tell us as well, that an increase in

the filler material as a volume fraction results in an increase in the probability of smaller distances for these particles.

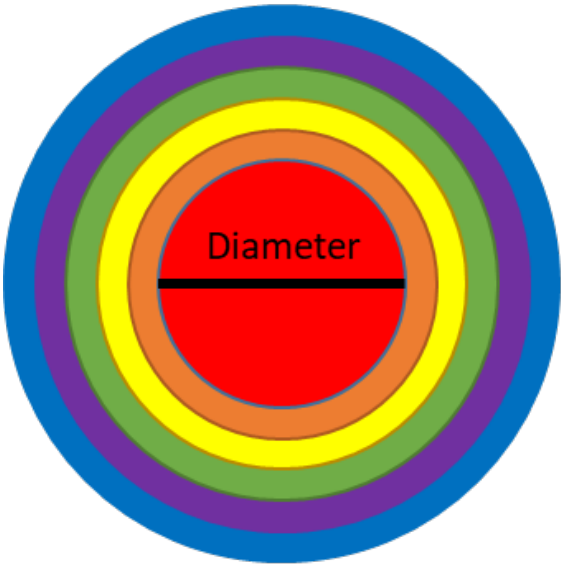

Nearest Neighbor	5-VF	25-VF	38-VF
(1%)D	1.3%	12%	27%
(1%-2%)D	1.3%	11%	20%
(2%-3%)D	1.4%	9%	15%
(3%-4%)D	0.8%	9%	11%
(4%-5%)D	1.4%	7%	8%
(>5%)D	93.8%	52%	19%

Figure 5.1: Probabilistic Distribution of Inter-Particle Distances

Now that we have a method for the determination of the probabilities that particles will lie within a certain range of one another, we can use this data to calculate the internal stresses of the particles and the effects this may have on the overall composites. These internal stresses will be solved for using two methods in this work. The first is an analytical approach that will implement an inter-particle contact stress using Hertzian Contact Theory [51]. The second method is a computational solution that uses three dimensional finite element simulations to determine the stress generated via inter-particle contacts and also examine the effects of minimal inter-particle distances.

Analytical Method

So we begin with the first method, the analytical method. For this method an analytical solution to the stresses generated via sphere to sphere contact will be used. There are several works (more than listed here) that have further explored the effects of sphere on sphere contact, and further perfected the original works of Hertz [61, 48, 62, 63]. Sphere to sphere contact equations will be used in conjunction with the modified Eshelby equations known as the Mori-Tanaka method [64, 65, 66]. Eshelby's theory determines the stress of a particle in an infinite matrix. The Mori-Tanaka is an iterative method that uses the properties of the composite as the matrix and then reuses the Eshelby method. This method will apply a third link to this by adding stresses that could be generated via inter-particle contacts. Let us start with an examination of Figure 5.2 below which shows the Mori-Tanaka Plotted with the experimental piezospectroscopic measurements.

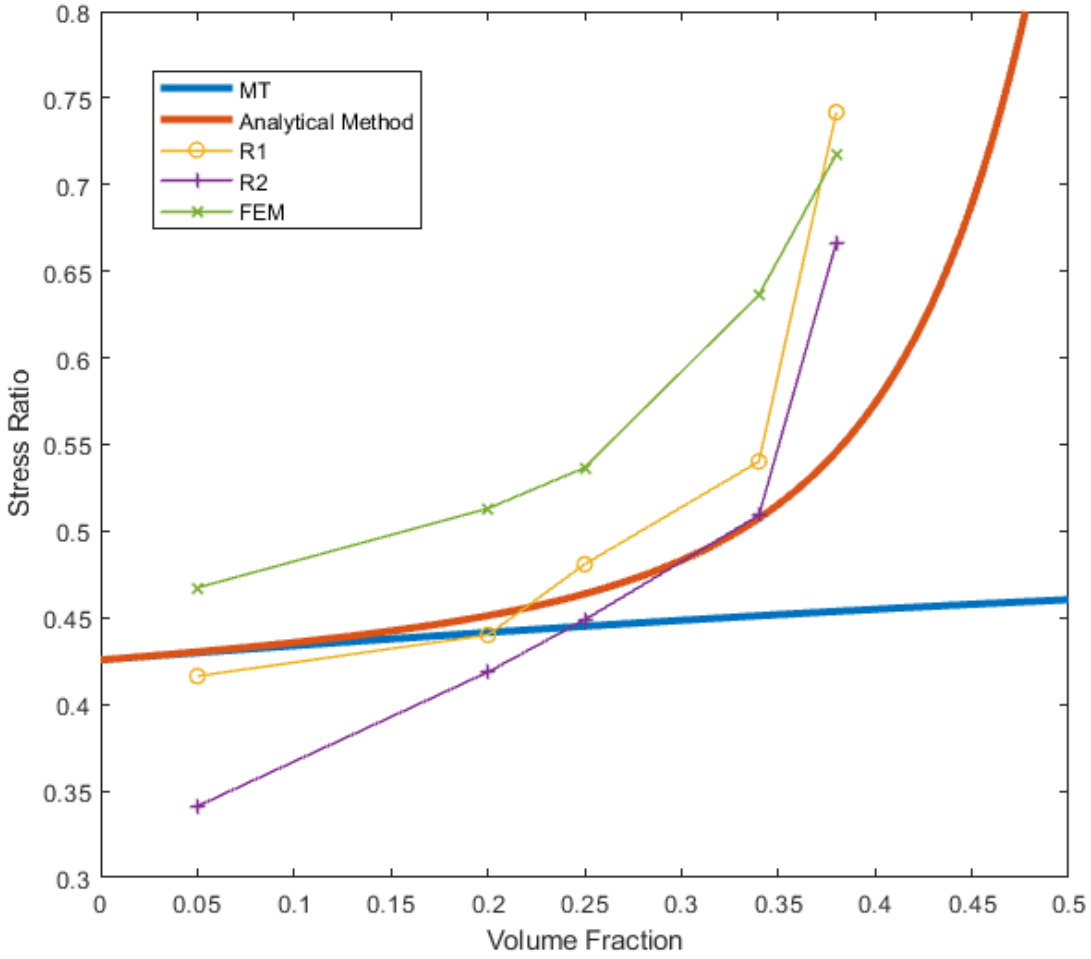

Figure 5.2: Comparison of Stress Ratio

As the volume fraction increases the predictive capabilities of load transfer as well as material properties tend to decrease. This could be due to overlooking the effect that the particles have on one another. A standard RVE (representative volume element) can be used to calculate these stresses. The volume of this element is 1, and there are two perfect spherical particles directly in

contact with one another. The radius of the spheres is calculated retroactively from the volume fraction and is represented by R. The compressive load applied to the RVE is normalized to 1. The percentage of stress induced in the particle or the stress ratio, which was calculated via the Mori-Tanaka Method will be represented by P. Material properties which matched the experimental values used ($E_a = 300, v_a = 0.2, E_e = 2.4, v_e = 0.4$). The radius of contact of the two spheres is given by a, max stress is p_o, and finally pressure distribution is given by p. Equation 5.1, 5.2 and 5.3 below can then be used to determine the stress induced via sphere to sphere contact.

$$a = \left(\frac{3PR}{4E'}\right)^3 \tag{5.1}$$

$$E' = 2\left(\frac{1 - v_a}{E_a}\right) \tag{5.2}$$

$$p(r) = p_0\sqrt{1 - \left(\frac{r}{a}\right)^2} \tag{5.3}$$

Now the problem is that a compressive load may not lead to a perfectly applied load between the two spheres. There is a chance that they could come into contact at an angle, in fact this is more likely. The probabilities of the angle of contact between the two spheres is a much simplistic problem. $\sin(x)$ or $\cos(x)$ can be used as the probability density function for the angle of contact between two circles. This problem is dealing with spheres so therefore the probability density function for the point of contact will be $\sin^2(x)$ or $\cos^2(x)$. The probability of the angle of contact was also accounted for in this analytical approach. A simplistic version of the set of equations used

to derive the stress in the particles can be given as:

$$\frac{\sigma_{Part}}{\sigma_{Comp}} = \sigma_{MT} + (P_{Contact} P_{Ang} \sigma_{Hert})_{1con} + (P_{Contact} P_{Ang} \sigma_{Hert})_{2con} + (P_{Contact} P_{Ang} \sigma_{Hert})_{3con} + \cdots \tag{5.4}$$

The left side of the equation is in fact the stress ratio, the percentage of load transferred to the particle. σ_{MT} is the stress ratio calculated via Mori-Tanaka method. The P terms are the terms that account for both the probability of contact and the probability of contact angle. σ_{Hert} is the term derived from hertzian contact theory and represents stress generated via sphere to sphere contact. This equation adds in the probability of 2 contacts, 3 contacts, and so on. The probabilities decrease significantly after 3 even in the higher volume fractions, to the point of negligibility. However we account for this solution we accounted for up to 6 for good measure. Probability density functions cannot yield a value for any one specific distance, but rather for a range of distances. Because of this contact was assumed for all particles that lie within 1% of the diameter of the particle. The results of this analytical solution can be seen in Figure 5.2. The general layout of the algorithm used for this analytical method, as well as the Hertz contact setup can be seen below in Figure 5.3.

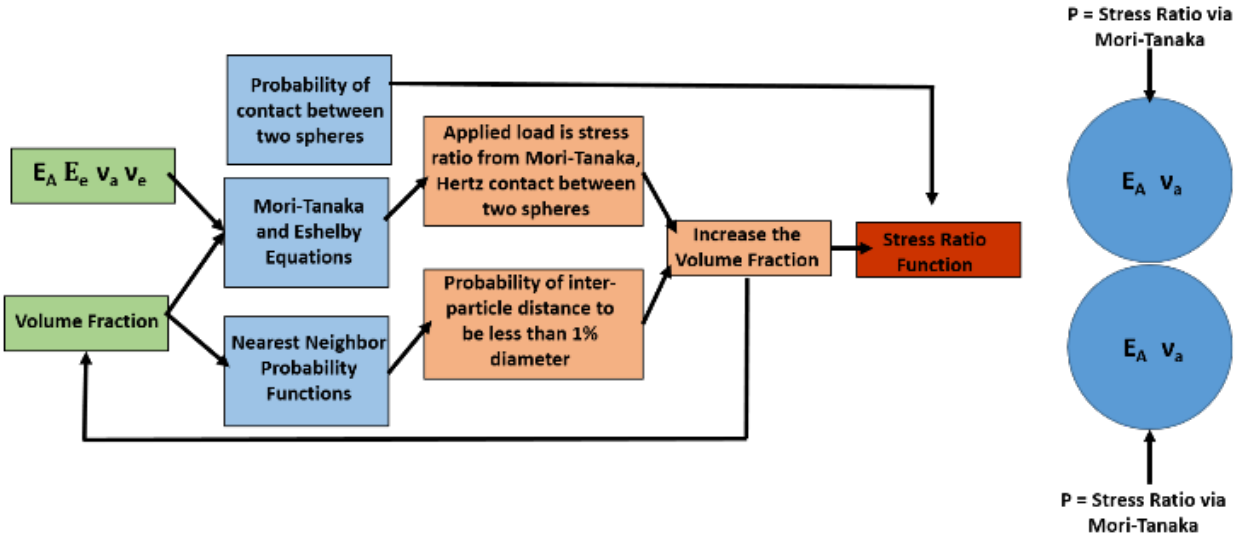

Figure 5.3: Algorithm for Analytical Method

Numerical Method

A similar probabilistic approach was taken for the finite element simulations for this study. Using the ”nearest neighbor functions” it is possible to determine the probabil-ity that a spherical particle is within a certain percentage of the diameter of a neighboring particle. This probability can be used as a weighted value on the stress that would be generated due to minimal distances between particles. So, just as these probabilities were used to weight the Hertzian contact stresses derived in Equation 5.4, they will again be implemented on stresses determined via finite element analysis (FEA). First we will describe the FEA conducted for this study and then describe how these studies were implemented into probabilistic equations. The geometric set up of the problem can be seen in Figure 5.4.

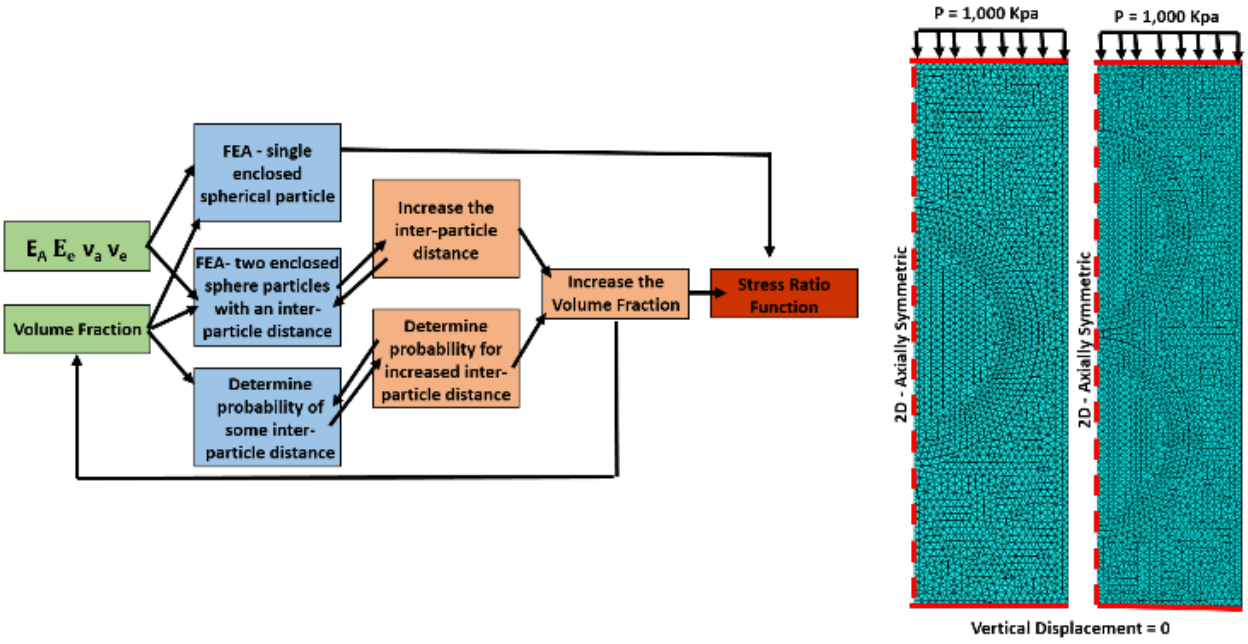

Figure 5.4: Algorithm for the FEA Method

The finite element software used for this study was ABAQUS. First a load of 1,000 kPa was applied to the top side of the cylinder. A boundary condition was applied to the bottom side to ensure 0 vertical displacement. The interface between the two materials used was cohesive. A triangular axisymmetric stress element was used for the mesh (CAX6M) with a quadratic solver. The mesh size was set to 0.01 nm, which usually led to around 7,000-10,000 elements. The time period was 1, initial step size 0.001, and maximum number of increments was set to 100,000. Upon completion of each simulation the average pressure of all of the alumina elements was taken, and with that pressure it was possible to solve for the stress ratio. The load of 1,000 Kpa was the denominator and the average pressure of the alumina spherical particles was the numerator. This can be seen of the left side of Equation 4 and 5. It can be mentioned now, that there was a simulation which only

had a single sphere inserted into the host cylinder, this was to determine the stress ratio numerically for situations where there was 0 interaction between particles. This term can been seen in Equation 5.5 as $\sigma_{SingleSphere}$.

In addition to a method to solve for the stress ratios of various inter-particle distances, it was also necessary to factor in the probability that these various distances would occur for a specific volume fraction of the alumina. The method used was the same as the analytical method, the probabilities were implemented into the equation as a weighting term for the stress generated due to minimal distance between particles. The probability of the angle of contact was also used a weighted term. The stress ratio determined for a single sphere simulation with no interacting particles is the first term in the equation ($\sigma_{SingleSphere}$). The probability that a particle exists within the range of 0%-1% of the diameter of another particle is listed as ($P_{0.01D}$) and the term ($P_{0.02D}$) signifies that a particle is in the range of 1%-2% of the diameter. The stress ratio from the FEA simulation that a particle is at a distance of 1% of the diameter of the opposing particle is $\sigma_{FEA-0.01D}$. The subscript is updated as the equation iterates and the inter-particle distance is increased.

$$\frac{\sigma_{Part}}{\sigma_{Comp}} = \sigma_{SingleSphere} + (P_{0.01D} P_{Ang} \sigma_{FEA-0.01D}) + (P_{0.02D} P_{Ang} \sigma_{FEA-0.02D}) + \cdots \tag{5.5}$$

The results for the finite element method can be viewed in Figure 5.2 and can be compared to the experimental data R1 and R2. For the finite element method, each specific volume fraction must be solved for using the algorithm given in Figure 5.4. In order to have direct comparison a total of 5 volume fractions were solved for, all of which were used in the experimental portion of this study: 5%, 20%, 25%, 34%, 38%. The lines are simply there to help guide the eye while comparing different data sets.

Conclusion/Discussion

The results from this work an increase in accuracy for prediction of the stress ratio for volume fractions which are above 25%. The Mori-Tanaka was used for this study, however there are several others that could have been used to predict the stress ratio such as Kims, Hashin-Strickman, and Voigt to name a few [67, 68, 69, 70]. These methods all have different strengths and weaknesses, however none were accurate for the entirety of the range of volume fractions. For this specific type of composite, a spherical nanoparticulate composite, a specific technique should be developed. Nanoparticle interaction could play a role in the mechanical behavior for a myriad of composites, especially when the percentage of nanoparticles is increased. In this study, two algorithms were developed to probe into the effect of inter-particle interactions on load transfer. One was analytical and the other was numerical. The analytical method shows a similar trend line to the experimental data. The reason that the analytical method trend line lags behind the experimental in the higher volume fractions could be due to the assumption of idealized spherical contact. The nanoparticles used in the experimental were not perfect spherical shapes. The FEA method predicts higher stress ratios across the board, until reaching into the higher volume fraction range. This may be improved if the increments between inter-particle distances were decreased. The overall purpose of these methods development was to probe into the differences in the stress ratio between experimental and current predictive techniques. Because both methods show more accurate results in the higher volume fractions, it could be concluded that the assumption that inter-particle interactions at higher volume fractions does have a direct effect on the stress ratio. This could be taken one step further to say to have an effect on the stress ratio is to have an effect on the other mechanical properties, such as modulus of elasticity and poisons ratio. To be able to predict the properties of this nanocomposite material, can lead to an increase in the efficiency in the characterization of these materials for the myriad of industries which utilize them.

CHAPTER 6: CONCLUSIONS AND FUTURE OUTLOOK

Acoustic thermography demonstrates the ability to determine the location and certain details of defects. This technique shows promise across a wide array of fields, due to the fact the an acoustic signal can be transmitted and recieved across a wide array of materials. A determination of the magnitude of contribution of both input signal and output signal for this technique is quite necessary for increasing the resolution of defect detection. Numerical computation can help to investigate these parameters in a more efficient manner than could be done experimentally. Although in situ measurements may not be possible for this particular technique, analysis of components during shutdown cycles could still be feasible. a signal could also be produced via a laser in the future, in order to make this method both non invasive and non destructive. The determination of the optimal parameters for laser type and settings is another area which is well suited to numerical computational analysis.

The PLPS study performed for this work also revealed key insights into the micromechanical behavior of a particulate material in a given host. Numerical computation used in conjunction with this PLPS measurement could provide health data about certain component, but could also provide insight into the mechanisms that contribute to a failure. The measurement of stress both non invasively and non destructivly also has potential in several other fields rather than just the ones proposed in this work. An embedded material is required to have optimal luminscence properties, and this process must be considered. Once embedded however, a great deal of information and detail about the mechanics of a system can become available. When this data is analyzed numerically, this can attribute to a reduction in the necessity for physical experimentation for the optimization of parameters.

It is absolutely clear the non destructive testing methods will play a critical role in the future of

the aerospace and power generation systems. The advancement of these NDT methods will most certainly lead to the advancement of the technology under investigation via NDT methods. It has been shown in this work that the utilization of numerical computation can attribute to an increase in the resolution, as well as understanding of several NDT methods. Constant health monitoring of complex machinery is a growing demand from industry, and this task will certainly require a substantial amount of analysis if it is to be completed. To summarize, non destructive testing methods must ultimately be used in conjunction numerical computation in order to investigate the mechanisms the contribute to the operation, success, and failure of a given system.

LIST OF REFERENCES

[1] C. Hellier, *Handbook of nondestructive evaluation*, vol. 10. Mcgraw-hill New York, 2001.

[2] D. McCann and M. Forde, "Review of ndt methods in the assessment of concrete and masonry structures," *Ndt & E International*, vol. 34, no. 2, pp. 71–84, 2001.

[3] B. Raj, T. Jayakumar, and M. Thavasimuthu, *Practical non-destructive testing*. Woodhead Publishing, 2002.

[4] J. Blitz and G. Simpson, *Ultrasonic methods of non-destructive testing*, vol. 2. Springer Science & Business Media, 1995.

[5] C. U. Grosse and M. Ohtsu, *Acoustic emission testing*. Springer Science & Business Media, 2008.

[6] M. Rothenfusser, C. Homma, P. J. Zombo, P. D. Vona, and R. E. Shannon, "Method for calibrating and enhancing flaw detection of an acoustic thermography system," June 20 2006. US Patent 7,064,331.

[7] C. Homma, M. Rothenfusser, J. Baumann, and R. Shannon, "Study of the heat generation mechanism in acoustic thermography," in *AIP conference proceedings*, vol. 820, pp. 566–573, AIP, 2006.

[8] J. Renshaw, J. C. Chen, S. D. Holland, and R. B. Thompson, "The sources of heat generation in vibrothermography," *NDT & E International*, vol. 44, no. 8, pp. 736–739, 2011.

[9] F. Mabrouki, M. Thomas, M. Genest, and A. Fahr, "Frictional heating model for efficient use of vibrothermography," *NDT & E International*, vol. 42, no. 5, pp. 345–352, 2009.

[10] M. J. Rothenfusser, J. F. Baumann, R. E. Shannon, and P. J. Zombo, "System and method for multiple mode flexible excitation in sonic infrared imaging," June 6 2006. US Patent 7,057,176.

[11] R. L. Thomas, L. D. Favro, X. Han, Z. Ouyang, H. Sui, G. Sun, P. J. Zombo, and R. E. Shannon, "Miniaturized contactless sonic ir device for remote non-destructive inspection," June 4 2002. US Patent 6,399,948.

[12] P. D. Vona, P. J. Zombo, and R. E. Shannon, "Self-aligning apparatus for acoustic thermography," Apr. 12 2005. US Patent 6,877,894.

[13] P. J. Zombo, J. F. Landy, J. L. Rose, S. E. Owens, F. Yan, and C. J. Borigo, "Guided wave thermography methods and systems for inspecting a structure," Aug. 9 2016. US Patent 9,410,853.

[14] J. Rantala, D. Wu, and G. Busse, "Amplitude-modulated lock-in vibrothermography for nde of polymers and composites," *Journal of Research in Nondestructive Evaluation*, vol. 7, no. 4, pp. 215–228, 1996.

[15] T. Zweschper, A. Dillenz, G. Riegert, D. Scherling, and G. Busse, "Ultrasound excited thermography using frequency modulated elastic waves," *Insight-Non-Destructive Testing and Condition Monitoring*, vol. 45, no. 3, pp. 178–182, 2003.

[16] M. Rothenfusser and C. Homma, "Acoustic thermography: vibrational modes of cracks and the mechanism of heat generation," in *AIP Conference Proceedings*, vol. 760, pp. 624–631, AIP, 2005.

[17] P. Zombo, "Mechanical ultrasonic and high frequency sonic device," Feb. 3 2004. US Patent 6,684,681.

[18] R. L. Thomas, L. D. Favro, X. Han, Z. Ouyang, H. Sui, and G. Sun, "Infrared imaging of ultrasonically excited subsurface defects in materials," May 22 2001. US Patent 6,236,049.

[19] P. Zombo, P. Vona, and M. A. Felix, "Reference standard systems for thermosonic flaw detection," June 13 2006. US Patent 7,060,971.

[20] A.-a. Saboktakin, C. Ibarra-Castanedo, A. H. Bendada, and X. Maldague, "Finite element analysis of heat generation in ultrasonic thermography," in *Proceedings of QIRT*, pp. 619–624, 2010.

[21] A. S. Rizi, S. Hedayatrasa, X. Maldague, and T. Vukhanh, "Fem modeling of ultrasonic vibrothermography of a damaged plate and qualitative study of heating mechanisms," *Infrared Physics & Technology*, vol. 61, pp. 101–110, 2013.

[22] A. Cavuto, F. Sopranzetti, M. Martarelli, and G. Revel, "Laser-ultrasonics wave generation and propagation fe model in metallic materials," *J Clin Exp Dent*, vol. 7, pp. 628–633, 2015.

[23] S. M. Shepard, T. Ahmed, and J. R. Lhota, "Experimental considerations in vibrothermography," in *Thermosense XXVI*, vol. 5405, pp. 332–336, International Society for Optics and Photonics, 2004.

[24] J. L. Rose, "Ultrasonic waves in solid media," 2000.

[25] Hibbitt, Karlsson, and Sorensen, *ABAQUS/Explicit: user's manual*, vol. 1. Hibbitt, Karlsson and Sorenson Incorporated, 2001.

[26] J. Whitehead, "Surface deformation and friction of metals at light loads," *Proc. R. Soc. Lond. A*, vol. 201, no. 1064, pp. 109–124, 1950.

[27] S. Nemat-Nasser, *Plasticity: a treatise on finite deformation of heterogeneous inelastic materials*. Cambridge University Press, 2004.

[28] S. Davies, C. Edwards, G. Taylor, and S. B. Palmer, "Laser-generated ultrasound: its properties, mechanisms and multifarious applications," *Journal of Physics D: Applied Physics*, vol. 26, no. 3, p. 329, 1993.

[29] D. Clorennec and D. Royer, "Analysis of surface acoustic wave propagation on a cylinder using laser ultrasonics," *Applied physics letters*, vol. 82, no. 25, pp. 4608–4610, 2003.

[30] J.-P. Monchalin, "Laser-ultrasonics: From the laboratory to industry," in *AIP Conference Proceedings*, vol. 700, pp. 3–31, AIP, 2004.

[31] C. B. Scruby and L. E. Drain, *Laser ultrasonics techniques and applications*. CRC Press, 1990.

[32] R. Courant, K. Friedrichs, and H. Lewy, "On the partial difference equations of mathematical physics," *IBM journal of Research and Development*, vol. 11, no. 2, pp. 215–234, 1967.

[33] H. P. Langtangen, *Computational partial differential equations: numerical methods and diffpack programming*, vol. 2. Springer Science & Business Media, 2013.

[34] D. L. McDanels, T. T. Serafini, and J. A. DiCarlo, "Polymer, metal, and ceramic matrix composites for advanced aircraft engine applications," *Journal of materials for energy systems*, vol. 8, no. 1, pp. 80–91, 1986.

[35] R. A. Vaia and J. F. Maguire, "Polymer nanocomposites with prescribed morphology: going beyond nanoparticle-filled polymers," *Chemistry of Materials*, vol. 19, no. 11, pp. 2736–2751, 2007.

[36] D. Carolan, A. Ivankovic, A. Kinloch, S. Sprenger, and A. Taylor, "Toughened carbon fibre-reinforced polymer composites with nanoparticle-modified epoxy matrices," *Journal of Materials Science*, vol. 52, no. 3, pp. 1767–1788, 2017.

[37] J. Barnett, S. Block, and G. Piermarini, "An optical fluorescence system for quantitative pressure measurement in the diamond-anvil cell," *Review of Scientific Instruments*, vol. 44, no. 1, pp. 1–9, 1973.

[38] S. Sridharan, L. Xie, E. H. Jordan, and M. Gell, "Stress variation with thermal cycling in the thermally grown oxide of an eb-pvd thermal barrier coating," *Surface and Coatings Technology*, vol. 179, no. 2-3, pp. 286–296, 2004.

[39] A. Stevenson, A. Jones, and S. Raghavan, "Stress-sensing nanomaterial calibrated with photostimulated luminescence emission," *Nano letters*, vol. 11, no. 8, pp. 3274–3278, 2011.

[40] H. M. Inglis, *Modeling the effect of debonding on the constitutive response of heterogeneous materials*. PhD thesis, University of Illinois at Urbana-Champaign, 2014.

[41] A. Stevenson, A. Jones, and S. Raghavan, "Characterization of particle dispersion and volume fraction in alumina-filled epoxy nanocomposites using photo-stimulated luminescence spectroscopy," *Polymer journal*, vol. 43, no. 11, p. 923, 2011.

[42] D. G. Lee, J. K. Kim, and D. H. Cho, "Effects of adhesive fillers on the strength of tubular single lap adhesive joints," *Journal of adhesion science and technology*, vol. 13, no. 11, pp. 1343–1360, 1999.

[43] D. Munson and K. Schuler, "Steady wave analysis of wave propagation in laminates and mechanical mixtures," *Journal of Composite Materials*, vol. 5, no. 3, pp. 286–304, 1971.

[44] A. International, *Standard Test Method for Compressive Properties of Rigid Plastics*. ASTM International, 2010.

[45] I. Hanhan, E. Durnberg, G. Freihofer, P. Akin, and S. Raghavan, "Portable piezospectroscopy system: non-contact in-situ stress sensing through high resolution photo-luminescent mapping," *Journal of Instrumentation*, vol. 9, no. 11, p. P11005, 2014.

[46] J. He and D. R. Clarke, "Determination of the piezospectroscopic coefficients for chromium-doped sapphire," *Journal of the American Ceramic Society*, vol. 78, no. 5, pp. 1347–1353, 1995.

[47] V. Gryaznov, M. Y. Tanakov, and L. Trusov, "Plasticity and mass-transfer in contacting nanoparticles," *Journal of materials science*, vol. 27, no. 18, pp. 4829–4841, 1992.

[48] K. Johnson, K. Kendall, and A. Roberts, "Surface energy and the contact of elastic solids," *Proc. R. Soc. Lond. A*, vol. 324, no. 1558, pp. 301–313, 1971.

[49] S. Torquato, *Random heterogeneous materials: microstructure and macroscopic properties*, vol. 16. Springer Science & Business Media, 2013.

[50] J. A. Greenwood and J. H. Tripp, "The elastic contact of rough spheres," *Journal of Applied Mechanics*, vol. 34, no. 1, pp. 153–159, 1967.

[51] A. Keyvani, M. Saremi, and M. H. Sohi, "Oxidation resistance of ysz-alumina composites compared to normal ysz tbc coatings at 1100 c," *Journal of alloys and compounds*, vol. 509, no. 33, pp. 8370–8377, 2011.

[52] A. Keyvani, M. Saremi, M. H. Sohi, Z. Valefi, M. Yeganeh, and A. Kobayashi, "Microstructural stability of nanostructured ysz–alumina composite tbc compared to conventional ysz coatings by means of oxidation and hot corrosion tests," *Journal of Alloys and Compounds*, vol. 600, pp. 151–158, 2014.

[53] S. R. Choi and N. P. Bansal, "Strength and fractue toughness of ysz/alumina composites for solid oxide fuel cells," in *26th Annual Conference on Composites, Advanced Ceramics, Materials, and Structures: A: Ceramic Engineering and Science Proceedings, Volume 23, Issue 3*, pp. 741–750, Wiley Online Library, 2002.

[54] G. J. Piermarini, S. Block, J. Barnett, and R. Forman, "Calibration of the pressure dependence of the r 1 ruby fluorescence line to 195 kbar," *Journal of Applied Physics*, vol. 46, no. 6, pp. 2774–2780, 1975.

[55] G. Freihofer, A. Schülzgen, and S. Raghavan, "Multiscale mechanics to determine nanocomposite elastic properties with piezospectroscopy," *Acta Materialia*, vol. 81, pp. 211–218, 2014.

[56] G. Freihofer, "Nanocomposite coating mechanics via piezospectroscopy," 2014.

[57] L. Grabner, "Spectroscopic technique for the measurement of residual stress in sintered al2o3," *Journal of Applied Physics*, vol. 49, no. 2, pp. 580–583, 1978.

[58] S. Torquato, T. M. Truskett, and P. G. Debenedetti, "Is random close packing of spheres well defined?," *Physical review letters*, vol. 84, no. 10, p. 2064, 2000.

[59] S. Torquato, "Mean nearest-neighbor distance in random packings of hard d-dimensional spheres," *Physical review letters*, vol. 74, no. 12, p. 2156, 1995.

[60] S. Torquato, "Nearest-neighbor statistics for packings of hard spheres and disks," *Physical Review E*, vol. 51, no. 4, p. 3170, 1995.

[61] H. Hertz, D. E. Jones, and G. A. Schott, *Miscellaneous papers*. Macmillan and Company, 1896.

[62] K. L. Johnson and K. L. Johnson, *Contact mechanics*. Cambridge university press, 1987.

[63] D. C. Lin, D. I. Shreiber, E. K. Dimitriadis, and F. Horkay, "Spherical indentation of soft matter beyond the hertzian regime: numerical and experimental validation of hyperelastic models," *Biomechanics and modeling in mechanobiology*, vol. 8, no. 5, p. 345, 2009.

[64] L. Kogut and I. Etsion, "Elastic-plastic contact analysis of a sphere and a rigid flat," *Journal of applied Mechanics*, vol. 69, no. 5, pp. 657–662, 2002.

[65] J. D. Eshelby, "The determination of the elastic field of an ellipsoidal inclusion, and related problems," *Proc. R. Soc. Lond. A*, vol. 241, no. 1226, pp. 376–396, 1957.

[66] T. Mori and K. Tanaka, "Average stress in matrix and average elastic energy of materials with misfitting inclusions," *Acta metallurgica*, vol. 21, no. 5, pp. 571–574, 1973.

[67] C. Wong and R. S. Bollampally, "Thermal conductivity, elastic modulus, and coefficient of thermal expansion of polymer composites filled with ceramic particles for electronic packaging," *Journal of Applied Polymer Science*, vol. 74, no. 14, pp. 3396–3403, 1999.

[68] M. Dunn and M. Taya, "Micromechanics predictions of the effective electroelastic moduli of piezoelectric composites," *International Journal of Solids and Structures*, vol. 30, no. 2, pp. 161–175, 1993.

[69] E. Kerner, "The elastic and thermo-elastic properties of composite media," *Proceedings of the physical society. Section B*, vol. 69, no. 8, p. 808, 1956.

[70] J. Kim and J.-K. Lee, "A new model to predict effective elastic constants of composites with spherical fillers," *Journal of mechanical science and technology*, vol. 20, no. 11, pp. 1891–1897, 2006.